2
High-Power Diode Laser Technology and Characteristics

Martin Behringer

2.1. Principles of Diode Laser Operation

Götz Erbert and Reinhard März

Laser operation relies on two conditions, stimulated emission of the amplifying medium and feedback by an optical resonator. The threshold of laser operation is obtained if the gain in the resonator compensates for the overall losses, i.e., the propagation losses and the apparent losses due to the extraction of light [2.1]. Both common laser conditions are satisfied in diode lasers in another way than in typical gas or solid-state lasers. The resonator is given by the semiconductor structure itself using the crystal facets as mirrors. The gain in diode lasers involves a whole crystal structure and not only excited single atoms, ions, or molecules. Modern semiconductor lasers restrict the excited volume to reduce the threshold current by applying quantum wells or quantum dots. Technically, this is achieved by growing very thin layers consisting of different crystal compositions for quantum wells or by applying two-dimensional growth for quantum dots. A scheme of a diode laser is shown in Fig. 2.1. The following chapter takes a short tour through the excitation of high-power semiconductor lasers by examining the current injection of carriers, the optical gain, and appropriate resonator structures. More detailed descriptions of several aspects can be found in several textbooks [2.2, 2.3].

The electronic states of crystals form energy bands (Fig. 2.2). At zero temperature, Pauli's principle results in band filling up to a certain level, the Fermi energy level. The status at finite temperatures is described by the Fermi function [2.4]. In semiconductor crystals, the Fermi level is always between two energy bands, the valence band and the conduction band. The minimum gap between both energy bands is called band gap. Semiconductors without impurities and distortions exhibit no allowed states in the band gap. For optoelectronics, direct semiconductors are normally used where the minimum energy of the conduction band and the maximum energy of the valence band are at the Γ-point, i.e., at the center of the Brillouin zone.

If an electron is lifted into the conduction band, e.g., by absorption of a photon, it will leave a hole in the valence band. The optical gain within a semiconductor laser

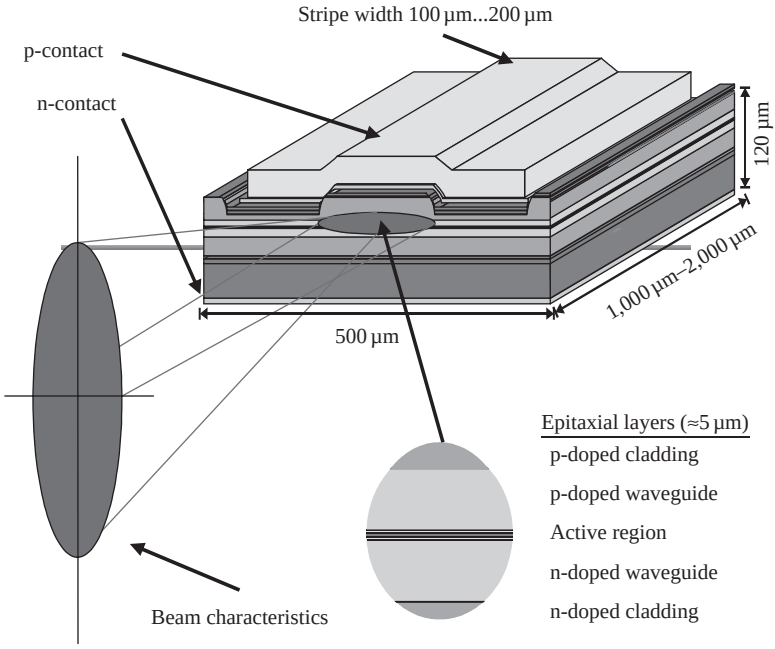

FIGURE 2.1. Schematic of a semiconductor diode stripe laser

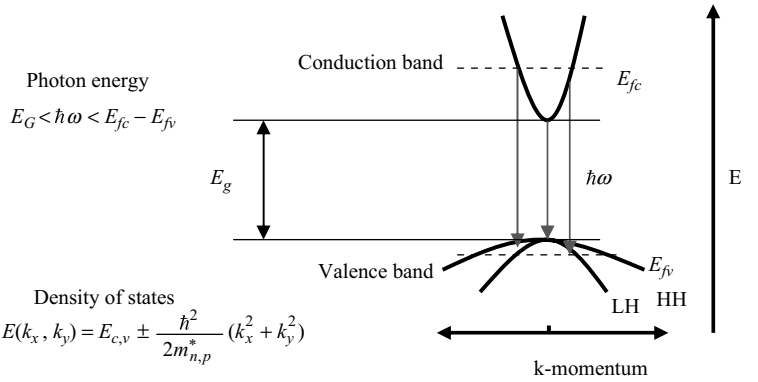

FIGURE 2.2. Band structure of a direct semiconductor crystal close to the Γ-point. The valence band is split into bands for light and heavy holes. E_g is the energy difference between valence and conduction band respectively. In unpumped material, the Fermi level is in the band gap, inversion pumped material can be described by so called quasi Fermi levels E_{fc} and E_{fv}

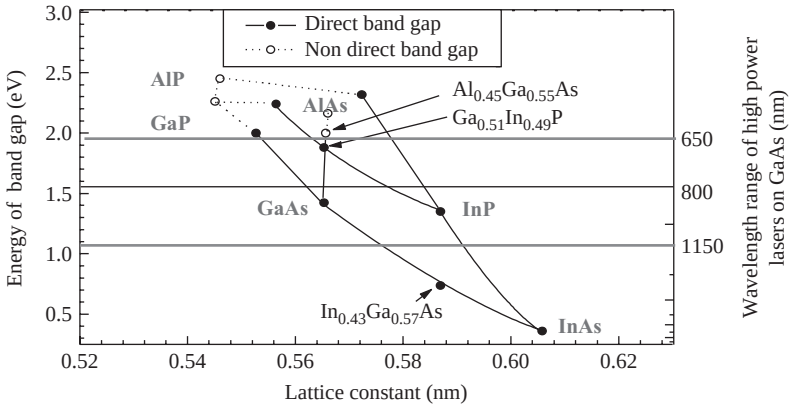

FIGURE 2.3. "Landscape" for laser design band gap of III/V compound semiconductors versus lattice constant

is then generated by radiative recombination of those electron–hole pairs. Direct semiconductors allow for the emission of a photon in a quantum-mechanical first-order process. Most III/V compound semiconductors exhibit direct band gaps, semiconductors such as silicon and germanium exhibit an indirect band structure and are therefore not suited for light-emitting optoelectronic components. The energy of the generated photon corresponds to the difference of the two energy levels. The wavelength of the semiconductor lasers is determined by the size of the band gap and in turn by the composition of the crystal. High-power semiconductor lasers emitting in the 0.7–1.0-μm-wavelength region are typically realized on GaAs and alloys lattice-matched to GaAs. Figure 2.3 shows the energy corresponding band gap versus the lattice constant.

Three crucial questions lead to a deeper understanding of stimulated emission in semiconductor lasers.

- How can a semiconductor crystal be most effectively pumped to generate optical gain?
- How can an excited semiconductor crystal be embedded in an optical resonator?
- How many electron-hole pairs are required to generate optical gain?

2.1.1. Optical Gain in Semiconductors

The first question concerns the generation of optical gain. Like gas and solid-state lasers, semiconductor lasers can be excited by photons of sufficient energy or by electron beams. However, the option to pump semiconductor diode lasers by applying an electrical current represents the main advantage of those devices compared to the competing technologies. Diode lasers make use of the conductivity of semiconductors by doping, i.e., by embedding impurity atoms with a higher or lower number of electrons in the outer shell. These atoms create new quantum-mechanical states within the band gap. If the new states are close to the edge of the

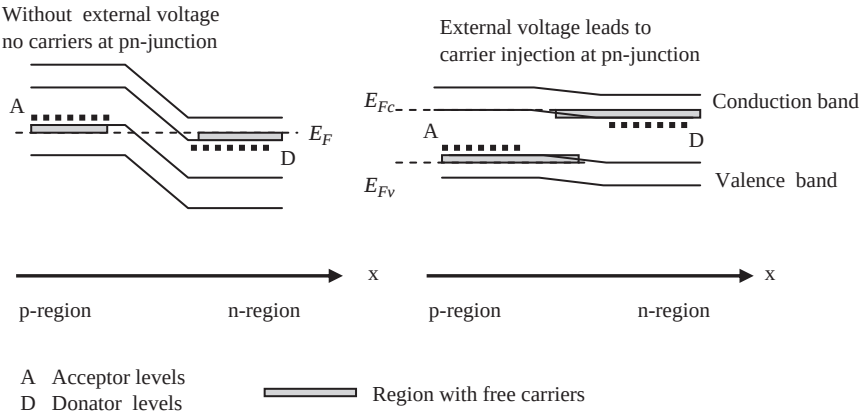

FIGURE 2.4. Recombination at the pn-junction of a semiconductor diode laser

valence band, the electrons will occupy these states, leaving holes in the valence band. This case is called p-doping, due to the fact that positively charged carriers are generated in the valence band which can carry a current. If, in contrast, the new states are close to the conduction band, electrons will be thermally excited to the conduction band. This case is called n-doping, because the negatively charged electrons will carry the current if a potential difference is applied. A diode laser, just like a normal diode, always consists of a p-doped part and an n-doped part (see Fig. 2.1). When a positive electrical potential is applied at the p-doped region, the holes will move to the n-doped region. A negative electrical potential at the n-doped region will drive the electrons to the p-doped part. The optical gain is generated at the pn-junction. At the junction an electron and a hole will recombine, creating one photon, i.e., the energy will be converted to light (see Fig. 2.4). To achieve a substantial current flow, the potential difference must be at least slightly above potential difference given by the band gap. If the injection level – typically at carrier density 10^{18} to 10^{19} cm^{-3} – is high enough, the generated photons exceed the loss.

First semiconductor diode lasers produced in the 1960s were simple homo-junction devices consisting of GaAs. The thickness of the active region was determined by the diffusion length, typically 2 μm. In modern semiconductor diode lasers, due to development of modern epitaxial growth methods, the active region is a quantum well; that means, a thin layer of about 10 nm is surrounded by material with a larger band gap. The injected carriers can now be captured in a very thin layer by the potential barriers of the larger band gap material. In Fig. 2.5, the distribution of the band gaps is shown for a typical modern semiconductor laser. The quantum well consists of InGaAs. The well is embedded in AlGaAs, a ternary alloy with larger band gap but nearly the same lattice constants as GaAs. The band gap offsets must deliver high enough barriers, typically >100 meV, for electrons and holes to have negligible leakage of carriers by thermal excitation (about 24 meV at room temperature).

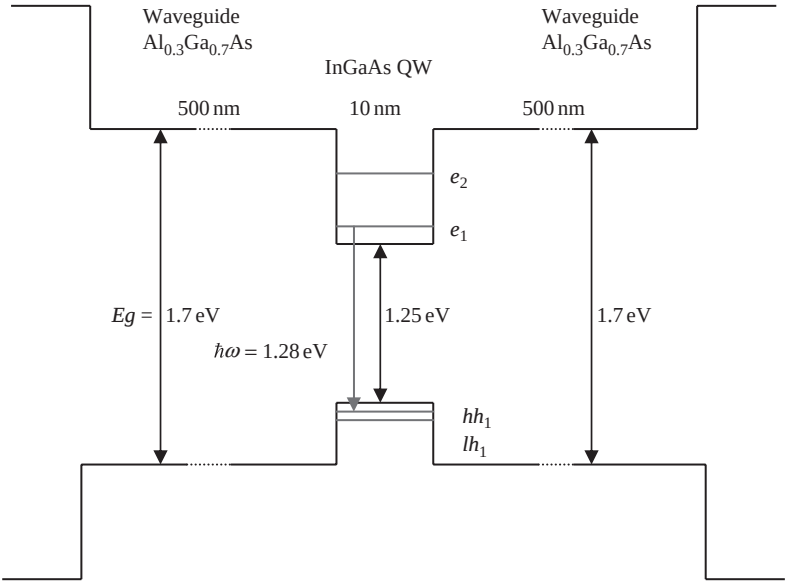

FIGURE 2.5. Band gap distribution and relevant energy levels of an InGaAs-QW embedded in a AlGaAs waveguide layers

Using a quantum well as active region has several advantages:

- First, since the band gap increases outside the quantum well (QW), only the QW-region has to be pumped to generate inversion. Since this volume is very small, the injection current density is reduced by about three orders of magnitude in comparison to homo-junction lasers.
- Second, the carriers are efficiently captured by the QW's barrier making it unnecessary to dope the regions close to the junction. The efficiency of radiative recombination reaches more than 90% in modern standard devices, material of highest quality allows for efficiencies of nearly 100%. On the other hand, the low doping results in laser structures with very low internal loss. As a consequence, QW's opened a way to long lasers of high external efficiency. The reduction of thermal and series resistance by lengthening the lasers up to 4 mm for single emitters and 2 mm for bars allows the high power of about 4 W of 100-μm stripe-single emitters and more than 50 W of laser bars, respectively.
- Third, the quantum well is a layer of about 10-nm thickness. Such thin layers allow for material compositions with lattice constant not fully matching that of GaAs. By replacing gallium partly (typically a few percent) with indium, the addressable wavelength range can be extended up to 1,100 nm. The introduced strain improves the distribution of density of states further and allows threshold current densities of typically 200 A/cm^2 for high-power semiconductor lasers. By replacing Arsenic with Phosphorous, the wavelength range can be extended down to 730 nm.

Table 2.1. Composition of QW and barrier layers for diode lasers emitting between 780 nm and 1060 nm

Wavelength	QW-material	QW thickness	Lattice mismatch	Polarisation	Barriers
780 nm	GaAsP	14 nm	0.8%	TM	$Al_{0.45}Ga_{0.55}As$
810 nm	GaAsP	15 nm	0.5%	TM	$Al_{0.45}Ga_{0.55}As$
810 nm	AlInGaAs	8 nm	1%	TE	$Al_{0.35}Ga_{0.65}As$
880 nm	$In_{0.08}Ga_{0.92}As$	7 nm	1%	TE	$Al_{0.45}Ga_{0.55}As$
940 nm	$In_{0.10}Ga_{0.90}As$	8 nm	1.2%	TE	$Al_{0.35}Ga_{0.65}As$
980 nm	$In_{0.12}Ga_{0.88}As$	10 nm	1.3%	TE	$Al_{0.35}Ga_{0.65}As$
1,060 nm	$In_{0.15}Ga_{0.85}As$	8 nm	1.5%	TE	$Al_{0.25}Ga_{0.75}As$

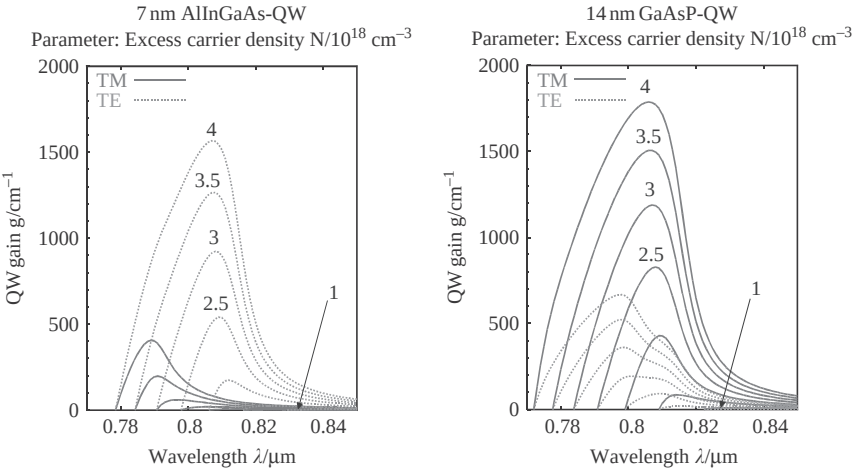

Figure 2.6. Calculated optical gain versus wavelength at different excitation levels for a compressively strained AlInGaAs-QW and a tensile-strained GaAsP-QW at 810 nm

For example, devices emitting at 808 nm, which are important for optical pumping of Nd–based solid-state lasers, can be produced by using compressively strained InAlGaAs or tensile-strained GaAsP-QWs. Table 2.1 shows compositions of QWs for the most interesting wavelengths.

Figure 2.6 shows the optical gain at different excitation levels versus wavelength at 810 nm for an AlInGaAs and GaAsP QW embedded in AlGaAs layers with higher band gap. The gain is calculated from the band structure.

The optical gain in the active material can reach values of more than 1,000 cm^{-1}. Since only a small part of the guided mode is confined in the QW (see next paragraph) the modal optical gain is much smaller, about 10 to 30 cm^{-1}. Despite this reduction the gain is still much higher than that of other lasers, especially that of typical solid-state lasers. The large gain allows for high mirror losses, i.e., light extraction of up to 95% even for extremely short resonator lengths of 1 to 2 mm.

From the figures it is seen that the optical gain increases sublinearly with carrier density. The density of states in a QW geometry increases in a step-like manner. The gain saturates at a given wavelength due to the limited number of states.

In laser design for practical estimations the gain g can be described by the following formula:

$$\text{Material gain in QW } g = g_0 \cdot \ln \frac{j}{j_{tr}} \tag{2.1}$$

where j stands for the current density applied to the devices. The reference gain g_0 and the transparency current j_{tr} are material constants depending on composition, thickness and strain value of the QW and barrier material, respectively. The current density is correlated with the carrier density by injection efficiency and carrier lifetime. Their values are in most practical cases near 100% and around 1 ns, respectively. Compressively strained In(Al)GaAs exhibits transparency currents between 50 and 100 A/cm^2 in the wavelength range 800 to 1060 nm. The values for tensile-strained GaAsP QWs at 800 nm are between 100 and 150 A/cm^2. On the other hand, the g_0 values for tensile-strained QWs are higher. The threshold current densities of tensile-strained or compressively strained QW lasers are similar.

The values of the optical gain g resulting from Eq. (2.1) describe only the material gain within the quantum well. The important value for the amplification of the optical wave within the resonator, the modal gain g_m, depends on the degree of overlap of the optical wave with the QW.

2.1.2. Optical Resonators

The optical resonator of a semiconductor diode laser consists of a waveguide structure between the mirrors build by crystal facet (Fig. 2.7).

These facets are coated to achieve the optimum reflectivity. In the vertical dimension, perpendicular to the pn-junction, the modal intensity distribution and the number of modes are determined by the thickness and composition of the grown layers. Waveguiding is supported for modes with two polarizations, one nearly transverse electric (TE) and one nearly transverse magnetic (TM). For

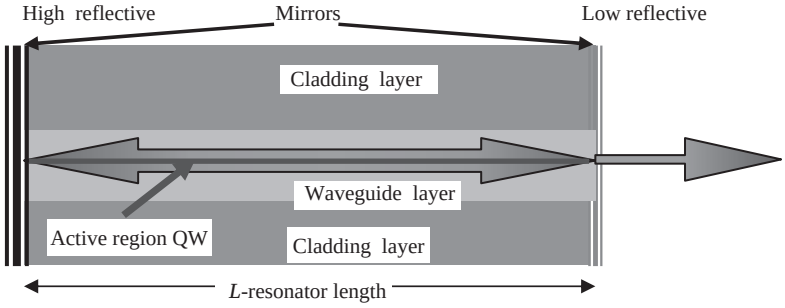

FIGURE 2.7. Schematic of diode laser optical resonator

the TE case, the electrical field vector oscillates parallel to the epitaxial layers; for the TM case the magnetic field vector. The polarization of the diode laser beam is determined by the kind of QW. Tensile-strained QWs yield more gain for TM modes, compressively strained QWs for TE-modes (see Fig. 2.6).

In the lateral direction the mode distribution is determined by geometrical aspects of the current injection and/or by lateral waveguide for example due to the etched waveguide structure. A broad contact stripe represents the most elementary structure from a fabrication point of view. "Broad" means that the lateral dimensions are large compared to both wavelengths and carrier diffusion length. Broad-Area (BA) diode lasers exhibit widths of around 100 µm corresponding to about 400 wavelengths and about 50 diffusion lengths, respectively. This broad lateral waveguide supports many guided modes resulting in the typical multimode beam characteristics of semiconductor diode lasers. Since nearly all recombination processes can contribute to the modal gain, the efficiency of such devices is very high. Measures to improve the lateral beam characteristics by mode selecting structures and the properties of such kind of diode lasers will be discussed in section 2.5.

2.1.2.1. Vertical Waveguide Structures

The vertical structure, an epitaxial layer structure, defines both an optical waveguide and a pn-junction by using the quantum well. The design of waveguide takes advantage of the increase of refractive index n with increasing band gap. This is illustrated in Fig. 2.8. AlAs exhibits $n = 2.9$ and GaAs 3.5. In comparison AlAs has a band gap energy of 2.9 eV and GaAs 1.4 eV. The active region has the highest refractive index and lowest band gap and allows thus for waveguiding. A single QW with a thickness of 10 nm is too thin to produce a good waveguide. As a consequence, the QW is embedded in a core region with material of higher refractive index and so-called cladding layers which have a lower refractive index.

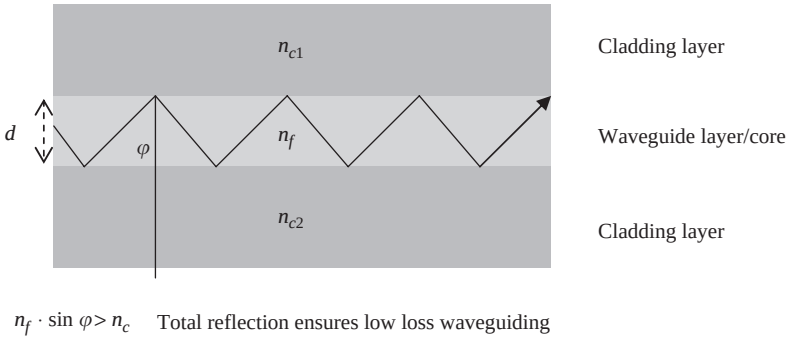

FIGURE 2.8. Schematic of a three layer waveguide: basic structure for diode lasers

These type of structures are designated as separate confinement heterostructures (SCH).

The thickness of the core and the refractive index difference between core and cladding layers determine the number of possible vertical modes and their distribution. For the core layer with a typical thickness between 0.5 μm to 2 μm the laser designer has the choice of different compositions of AlGaAs or AlInGaAsP, which must be lattice-matched to GaAs. The core layer is surrounded by cladding layers with a lower refractive index with a higher content of Al or P, respectively.

The waveguide design is an optimization to satisfy several partly detrimental demands for high-power, high-efficiency diode lasers. For TE-modes, the confinement factor Γ

$$\Gamma = \frac{\int_0^d E(x) \cdot E^*(x)dx}{\int_{-\infty}^{\infty} E(x) \cdot E^*(x)dx} \tag{2.2}$$

with thickness d of the quantum well and the local electrical field E describes the portion of the power of the propagating mode guided in the QW. For TM polarization, the formula is similar but slightly more complicated. Obviously, a high confinement factor ensures a high modal gain g_m. required for efficient laser operation. In fact, the modal gain $g_m = \Gamma \cdot g$ is given by the product of material gain and the confinement factor.

However, a very strong confinement of the light results in a high facet load and large beam divergence. For high-power diode lasers these parameters are critical with respect to reliability. As a rule of thumb, it is much easier to create lasers that withstand 5 to 10 MW/cm^2 on the facet for a short time than lasers that exhibit lifetimes of more than 10,000 h. In addition, a large beam divergence makes highly efficient, low-cost beam shaping nearly impossible.

Third, the layer structure is responsible for the series and thermal resistances. A high wall plug efficiency and good thermal stability requires a strong confinement of the optical wave in a thin layer structure.

Currently, a variety of waveguide structures are used to deal with these requirements. The optimal compositions and layer thickness depend on wavelength, the desired power, divergence, and wall plug efficiency. Figure 2.9 shows a layer structure for a high-power diode lasers emitting at 800 nm. The active region is a tensile-strained GaAsP-QW with a relatively large thickness of 15 nm. The core layer consists of $Al_{0.45}Ga_{0.65}As$. The cladding layers have an AlAs content of 70%. A small core thickness of 0.5 μm results in a smaller spot size and a larger confinement factor and, in turn, in a lower threshold current. On the other hand, the beam divergence and facet load can be reduced drastically by enlarging the core thickness. Higher-order modes will also exist for a core thickness above 1 μm. Due to their lower modal gain, these modes will never pass the threshold. Using a long resonator of about 2 mm and a thick GaAsP-QW delivering a high gain, lasers with core thickness upto 2 μm can be realized at high efficiency (LOC = large optical cavity).

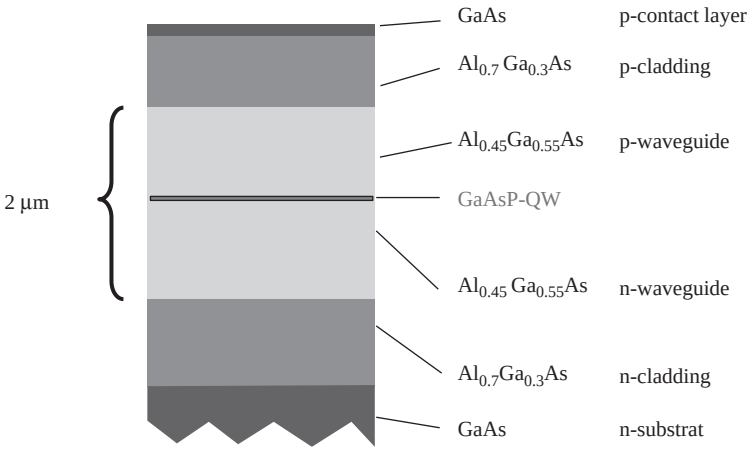

FIGURE 2.9. Schematic of layer structure of high-power 810-nm diode laser

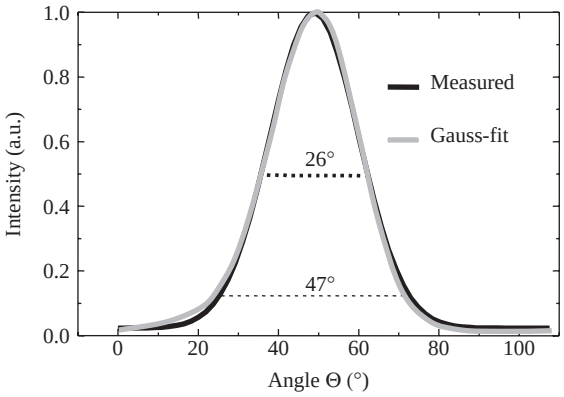

FIGURE 2.10. Intensity distribution of vertical beam of large optical cavity (LOC) diode laser

The distribution of optical intensity of the lowest-order mode inside the waveguide and the resulting intensity distribution for the far field are depicted in Fig. 2.10.

Waveguides with a large core diameter offer low-facet load and low numerical aperture (NA). Typically, 95% of the optical power is fed at an angle $<50°$, which in turn allows for the use of cost-efficient optical systems for collimation.

On the other hand, if a high wall plug efficiency of the diodes themselves represents the crucial requirement specification, e.g., for pumping solid-state lasers, the core thickness is reduced to obtain higher modal gain and reduced threshold current.

2.1.2.2. Lateral Waveguide Structures

In comparison to vertical optical waveguiding determined by the epitaxial layer system the optimization of lateral waveguiding is significantly more challenging. Generally, the effective refractive index is given by the layer structure. The value is typically close to the value of the refractive index of the core layer. Any impact on refractive index of one layer of the waveguide structure will change the effective refractive index. For mathematical description in a first and usually sufficient approximation, the impact on one layer must be multiplied with the confinement factor of this layer get the impact on the effective index. The waveguiding can be described like that of to the vertical structure if we assume that this effective index varies in lateral dimension, resulting in a "core" and "cladding" similar to usual waveguides. For high-power diode lasers the main interest is having only a weak waveguiding. Weak waveguiding allows larger dimensions for the fundamental mode and therefore lower facet load and higher output power. In the multimode case, the divergence will be smaller. In comparison to vertical waveguiding, the change in refractive index of the lateral waveguide core to the cladding is a magnitude lower that means typical around 10^{-3}.

In the case of broad-area lasers, the layer structure does not change in the lateral direction. The impact on effective index is given by the injection current only. The injection current causes the accumulation of carriers in the QW. The higher carrier density depresses the refractive index. Filling the higher band level by carriers leads to lower absorption and of course at the lasing wavelength to optical gain. Due to the common Kramers–Kronig relation this results in a reduction of the refractive index. A second effect is described by the Drude formula that free carriers due to plasma effects reduce the refractive index.

On the other hand, due to the series resistance, and non-radiative recombination, the temperature of the layer structure is rising up by several kelvin in dependence of thermal resistance. The refractive index increases with temperature roughly by 3.10^{-4}.

Both effects change the effective index by 10^{-4} to 10^{-3} but work against each other. So the behavior of broad area devices is not clearly predictable and changes especially with operating conditions. At threshold the carrier effect dominates typically. We have gain but "anti-guiding" caused by the index depression. In general we speak of "gain-guided" devices. The "anti-guiding" leads to optical loss and results in a slight drop in efficiency near the threshold.

Since the carrier density is clamped at threshold the heating effect dominates at operation levels high above threshold. The index depression is overbalanced and we have "normal" index guiding by the higher refractive index in the region of current injection. The efficiency increases slightly but the lateral divergence in general too.

Changing the layer structure in lateral direction a fixed effective index step can be created. One of the easiest ways is to etch the p-side cladding and partly the waveguide layer away. If we replace it by a material with lower index, typically Al_2O_3 or Si_3N_4 are used, the effective index is reduced. A schematic view is given in Fig. 2.11.

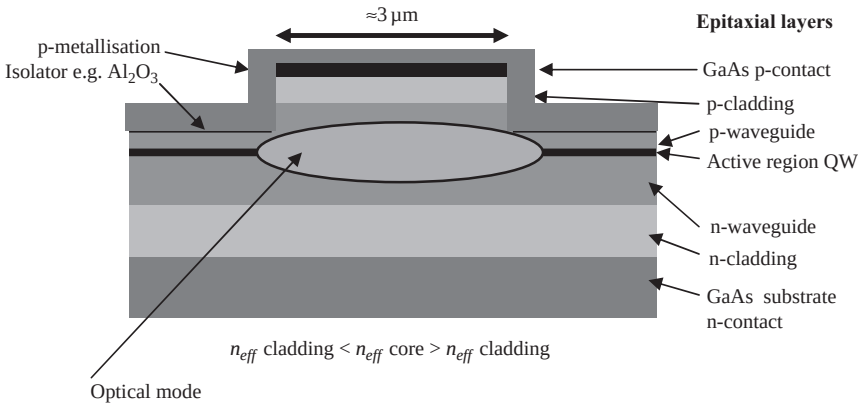

FIGURE 2.11. Schematic of a ridge waveguide structure

The refractive index difference is determined by the etching depth. It should be high enough that the impact on index under operating conditions can be neglected, but on the other hand small enough to achieve at least a few microns for the width of the fundamental mode. In high-power devices such structures were mainly used as mode selection filters in so called tapered lasers described in Chapter 2.5.

2.1.2.3. Longitudinal Modes and Spectral Behavior

The mirrors of a diode laser are fabricated by cleaving the semiconductor crystal perpendicular to stripes and coating the facets. This process delivers nearly ideal plane mirrors and ensures a high crystalline quality. As a consequence, high-power diode lasers are embedded in nearly perfect Fabry–Perot resonators with a highly reflecting mirror on the rear side and a low reflecting mirror on the front side for light extraction. The high material gain allows for a large light extraction. Currently, typical front mirrors exhibit reflectivities of ≈10% for devices with a length of 1 mm, 5% for 2 mm, and even 2% for devices with a length of 4 mm. The low reflectivity of the output mirror ensures a high wall plug efficiency at the expense of an increased sensitivity to optical feedback. Optical feedback may degrade the beam characteristics and modify the spectral behavior.

The resonator length defines the longitudinal mode spacing, adjacent modes are typically of 0.05 nm apart from each other. The spectral width of diode lasers is mainly determined by the gain spectrum. In addition, the gain spectrum is homogeneously broadened due to the high relaxation velocity within the conduction and valence band. Ridge waveguide lasers and partly tapered lasers (see Chapter 2.5) can be operated in a single longitudinal mode. However, the stability of this operating point is poor since the thresholds of adjacent modes are close to each other and upon weak changes in current, temperature or feedback mode hopping will appear. An additional mode filter is required to stabilize the single longitudinal mode regime. Such filters rely on more sophisticated chip technologies and/or additional external cavities. The additional fabrication costs prevent up to now

their use in commercial high-power diode lasers for material processing. Due to the large number of excited modes in broad area devices their spectral width is typically 1 to 2 nm.

2.1.3. Overview – Laser Basics

In the following a set of useful formulas for the description of high-power semiconductor lasers will be given. These formulas are based on relatively simple approximations, but they can give quick hints for understanding and optimization. For detailed descriptions there are several review articles and textbooks available.

Important formulas start with the equation for the lasing threshold in diode lasers with a Fabry–Perot resonator. At threshold the current density must be high enough so that the gain can compensate the internal loss α_i and mirror losses α_m.

$$g_{th} = \Gamma \cdot g_0 \cdot \ln\left(\frac{j_{th}}{j_T}\right) = \alpha_i + \alpha_m = \alpha_i + \frac{1}{L} \ln \frac{1}{R_f \cdot R_r} \tag{2.3}$$

R_f and R_r are the reflectivities of the front and the rear coupling mirrors, respectively. α_i is the value of internal losses, which stems mainly from free carrier absorption. Free carriers are necessary for the current flow. There is a trade off between series resistance and internal loss. It is an optimization process for doping level and light distribution to get a low internal loss. High-power devices achieve losses below $2\,\mathrm{cm}^{-1}$ down to $0.5\,\mathrm{cm}^{-1}$. L is the resonator length. From the equation it can be calculated straightforwardly that with gain values of about $10\,\mathrm{cm}^{-1}$ a threshold with very low values of R_f using a resonator length of 2 mm and longer can be reached. For 2-mm-long devices typical threshold current densities are between $100\,\mathrm{A/cm}^2$ and $200\,\mathrm{A/cm}^2$ at 900 nm and longer wavelengths and between $200\,\mathrm{A/cm}^2$ and $300\,\mathrm{A/cm}^2$ at around 800 nm.

The dependence of output power on pumping current above threshold can be described by a linear relation (2.4).

$$P_{opt} = \eta_d \cdot \frac{\hbar \cdot \omega}{q} \cdot (I_{op} - I_{th}) \tag{2.4}$$

$$\eta_d U = \eta_i \cdot \frac{\alpha_m}{\alpha_m + \alpha_i} \tag{2.5}$$

η_d is the so-called slope efficiency (Eq. (2.5)). To compare diode lasers at different wavelengths it is given by a dimensionless figure. It depends as usual for lasers on the relation between out coupling loss (mirror loss) α_m to the sum of internal losses α_i and out coupling losses multiplied by the efficiency of pumping, the so called internal efficiency η_i. For example if one has a gain of $10\,\mathrm{cm}^{-1}$ available and an internal loss of $2\,\mathrm{cm}^{-1}$ the laser can have mirror loss of $8\,\mathrm{cm}^{-1}$. Such configuration will result in a slope efficiency of 80%. The second factor in Eq. (2.4) gives the wavelength dependent normalization (photon energy divided by elementary charge).

An important factor in getting high-power from the small foot print of a semiconductor laser is the wall plug or better conversion efficiency η_c, the quotient of optical output power to electrical input power.

$$\eta_c = \frac{P_{opt}}{I_{op} \cdot U} = \eta_d \cdot \frac{\hbar \cdot \omega}{q} \cdot \frac{(I_{op} - I_{th})}{I_{op} \cdot (U_d + I_{op} \cdot R_s)}$$

$$= \eta_i \cdot \frac{\alpha_m}{(\alpha_m + \alpha_i)} \cdot \frac{\hbar\omega}{q \cdot (U_d + I_{op} \cdot R_s)} \cdot \frac{(I_{op} - I_{th})}{I_{op}} \tag{2.6}$$

To get a clear view of the physical background this relation can be split in four factors (last part of Eq. (2.6)).

The first factor η_i describes the pumping efficiency. The second gives the relation of output coupling to the total resonator losses. The third factor stands for the relation between the necessary voltage to get current injection to the real voltage of the device. This value includes the additional voltage due to the series resistance inside and outside of the chip. The last factor describes how far above threshold the laser works. Whereas the first factor is near one, that means nearly 100% of injected carriers will create lasing photons inside the resonator, for the other three we have values around 80% which results in a conversion efficiency of typically 50% for high-power diode lasers. Due to the fact that the ohmic loss grows quadratic with current, there exists a maximum for the conversion efficiencies at a certain operating current or equivalent output power. Therefore the development of optimized high-power diode lasers is coupled to the output power target.

Up to now thermal properties of diode lasers were not included. Temperature has an impact on threshold and differential efficiency mainly. The influence on thermal and electrical conductance is not so strong and normally neglected.

Phenomenologically the temperature dependence of threshold current and slope efficiency can be described with the help of exponential functions and two specific constants, T_0 and T_1 – see Eqs. (2.7) and (2.8).

$$I_{th}(T_{j2}) = I_{th}(T_{j1}) \cdot e^{\frac{T_{j2} - T_{j1}}{T_0}} \tag{2.7}$$

$$\eta_d(T_{j2}) = \eta_d(T_{j1}) \cdot e^{\frac{T_{j2} - T_{j1}}{T_1}} \tag{2.8}$$

Here, I_{th} and η_d are measured at the different junction temperatures T_{j1} and T_{j2}. It is very difficult to get values for T_0 and T_1 from first principles, but relatively simple to extract them from measurements. For practical use these constants are determined for every type of diode lasers. There are some common design rules, that high barriers and lower threshold current densities will increase both values, giving lasers with better temperature stability. Typical values are 100 K to 150 K for T_0 and 500 K and more for T_1.

This temperature dependence and the thermal resistance have to be included for an optimization of laser design for high efficiency at high-power output. A simulation process is introduced in the next subsection.

2.1.4. Modeling of Semiconductor Lasers

The efficiency model presented here is primarily designed for optimizing a laser diode, which is based on a given waveguide cross section by adapting the length of its resonator and the reflectance of its front facet and by applying an appropriate operating current. The model is formulated in terms of the differential quantities, i.e., gain, loss, currents, resistances, and power densities are related to infinitely thin slices of the laser resonator. Within the framework of such a theory, it is straightforward to formulate also the wall plug efficiency

$$\eta_W(\Delta T,\ \alpha_m,\ j) = p_{opt}(\Delta T,\ \alpha_m,\ j)/p_{el}(j) \tag{2.9}$$

in terms of the emitted optical power density $p_{opt}(\Delta T,\ \alpha_m,\ j)$ and the applied electrical power density $p_{el}(j)$. Three external parameters are used within the model. ΔT describes the temperature difference between heat sink and active region. For the case of a perfectly reflecting rear facet of the resonator, the loss coefficient is given as $\alpha_m = -\ln(R)/(2L)$, where R stands for the reflectance of the front facet and L for the length of the resonator. The line current density j applied to the laser forms the third external parameter. The electric model

$$p_{el}(j) = U_o j + \rho_s j^2 \tag{2.10}$$

relates the applied electrical power density to the voltage U_o at the pn-junction and to the series resistance ρ_s of the laser diode. The optical model [2.5] consists of three equations

$$p_{opt}(\Delta T,\ \alpha_m,\ j) = \eta_d(\Delta T,\ \alpha_m) \cdot [j - j_l - j_{th}(\Delta T,\ \alpha_m)] \tag{2.11}$$

$$\eta_d(\Delta T,\ \alpha_m) = \eta_i(\Delta T)\alpha_m/[\alpha_i(\Delta T) + \alpha_m] \tag{2.12}$$

$$j_{th}(\Delta T,\ \alpha_m) = j_{tr}(\Delta T) \cdot \exp\{[\alpha_i(\Delta T) + \alpha_m]/g_o(\Delta T)\} \tag{2.13}$$

relating the density of the emitted optical power to the differential quantum efficiency $\eta_d(\Delta T,\ \alpha_m)$ and the threshold current density $j_{th}(\Delta T,\ \alpha_m)$. The fixed parameters of the model – the transparency current density $j_{tr}(\Delta T)$, the internal quantum efficiency $\eta_i(\Delta T)$, the modal loss and gain coefficients $\alpha_i(\Delta T)$ and $g_o(\Delta T)$ – which are not subject to the optimization process, are given by $j_{tr}(\Delta T) = j_{tr}(0)\exp(\Delta T/T_{tr})$, $\eta_i(\Delta T) = \eta_i(0)\exp(-\Delta T/T_\eta)$, $\alpha_i(\Delta T) = \alpha_i(0)\exp(\Delta T/T_\alpha)$ and $g_o(\Delta T) = g_o(0)\exp(-\Delta T/T_g)$, where the T_{tr}, T_η, T_α, T_g represent the corresponding characteristic temperatures [2.6]. In Eq. (2.11), the leakage current density j_l acts as a simple offset. The thermal model describes the power dissipation

$$p_{el}(j) = p_{opt}(\Delta T,\ \alpha_m, j) + \Delta T/\rho_T \tag{2.14}$$

caused by the heat transfer to the heat sink. It allows to compute the thermal rollover of the laser diode and the temperature increase of the active region of the laser diode in comparison to the heat sink [2.7]–[2.10].

The computation of the optimum wall plug efficiency $\eta_W^{(max)}$ is equivalent to searching zeros in a four-dimensional ($\Delta T,\ \alpha_m,\ j,\ \chi$) parameter space, i.e.,

$$\frac{\partial p_{opt}}{\partial \Delta T}[1 + \chi \rho_T p_{el}] + \chi p_{el} = 0 \tag{2.15}$$

$$\frac{\partial p_{opt}}{\partial \alpha_m}[1 + \chi \rho_T p_{el}] = 0 \tag{2.16}$$

$$\frac{\partial p_{opt}}{\partial j}[1 + \chi \rho_T p_{el}] - \frac{\partial p_{el}}{\partial j}[n_W + \chi \rho_T p_{el}] = 0 \tag{2.17}$$

$$p_{el} - p_{opt} - \Delta T/\rho_T = 0 \tag{2.18}$$

where χ represents a Lagrange multiplier introduced to account for the power conservation (Eq. (2.15)). Equations (2.15) and (2.16) both include a term $[1 + \chi \rho_T p_{el}(j)]$. It can easily be shown that this term can never vanish i.e., Eq. (2.16) can be simplified to $\delta P_{opt}/\delta \alpha_m = 0$ and used to express the line current density in terms of ΔT and α_m. It is now straightforward to eliminate the Lagrange multiplier χ by using Eq. (2.15). The final expressions for these quantities are:

$$j = j_{th} - \eta_d \frac{\partial j_{th}}{\partial \alpha_m} \Bigg/ \frac{\partial (1/\eta_d)}{\partial \alpha_m} \tag{2.19}$$

$$\chi = -\eta_W / \left\{ \left[\frac{\partial \ln(p_{opt})}{\partial \Delta T} \right]^{-1} + \rho_T p_{opt} \right\}. \tag{2.20}$$

The zeros in the remaining two-dimensional ($\Delta T,\ \alpha_m$) parameter space must be computed by solving the remaining Eqs. (2.17) and (2.18) numerically.

2.1.5. Laser Characteristic

The computation of the laser characteristic yields a deeper insight into the optimization process. Figure 2.12 shows these characteristics for a high-power laser emitting at 808 nm (see Table 2.3 for the device parameters). The loss coefficient $\alpha_m = 0.30\,\mathrm{mm}^{-1}$ of the device as well as the temperature difference $\Delta T = 9.4\,\mathrm{K}$ between heat sink and active region and the line current density at the optimum operating point (oop) $j_{oop} = 1.57\,\mathrm{A/mm}$ is obtained from the optimization process described above. Along the laser characteristic, the temperature difference ΔT vs. current density is computed by using Eq. (2.18).

Figure 2.12 shows the optical power density p_{opt} as well as the wall plug efficiency η_W and the temperature difference ΔT between heat sink and active region as a function of the current density j applied to the laser. It becomes apparent that the optimum wall plug efficiency is obtained far away from the rollover (ro) $j_{ro} = 7.7\,\mathrm{A/mm}$. Furthermore, the wall plug efficiency drops sharply for current densities below the optimum $j < j_{oop}$ and the temperature difference increases dramatically up to $\Delta T_{ro} = 89.2\,\mathrm{K}$ at the rollover. These results indicate that the operation of the device close to the efficiency optimum helps

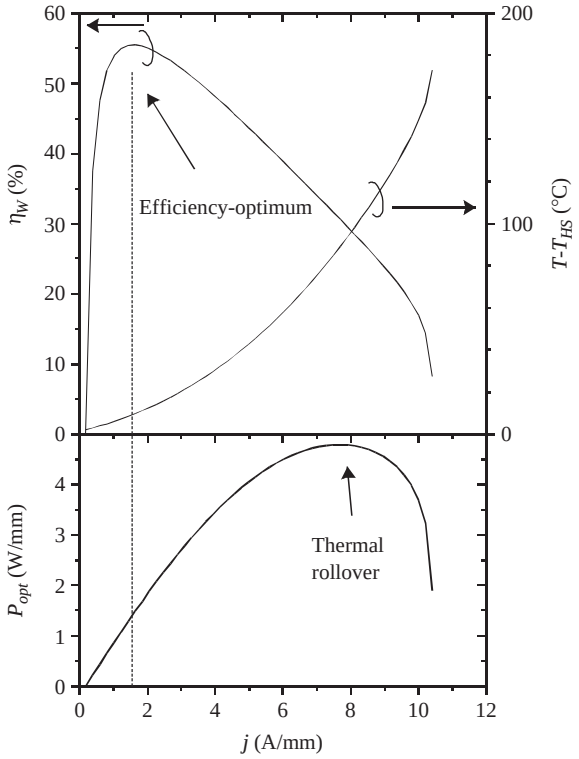

FIGURE 2.12. Optical power density p_{opt}, wall plug efficiency η_W and the temperature difference ΔT between heat sink and active region as a function of the current density j applied to a high-power laser operated at 808 nm

to prevent the devices from thermal stress which in turn results in device degradation.

The change of the wall plug efficiency caused by a varying operating current density j (at constant device length) is given by

$$\left[\frac{\delta\eta_W}{\delta j}\right]^{(N)} = \frac{j_l + j_{th}}{j - (j_l + j_{th})} - \frac{\rho_S j}{U_o + \rho_S j} \tag{2.21}$$

$$\left[\frac{d\eta_W}{dj}\right]^{(N)} = \left[\frac{\delta\eta_W}{\delta j}\right]^{(N)} - \frac{\rho_T j(U_o + 2\rho_S j - \eta_d)}{p_{opt}\left(\rho_T + \left[\frac{\delta p_{opt}}{\delta \Delta T}\right]^{-1}\right)}. \tag{2.22}$$

Equation (2.21) shows that the normalized derivative $[\delta\eta_W/\delta j]^{(N)}$ contains one positive and one negative term. Obviously, the positive term dominates for line current densities close to the threshold. The second, negative term which is driven by the series resistance increases with increasing line current density. The change of the device temperature along the laser characteristic, yields a second, decreasing

contribution which also gains importance with an increasing line current density. This contribution is driven by the thermal resistance.

2.1.6. Measurement of Parameters

To study the properties of real lasers, it is necessary to measure the model parameters. The intrinsic optical parameters, i.e., $\alpha_i(\Delta T = 0)$, T_α, $\eta_i(\Delta T = 0)$, T_η, $j_{tr}(\Delta T = 0)$, T_{tr}, $g_o(\Delta T = 0)$, T_g can be extracted by measuring threshold current and differential efficiency of equivalent uncoated (uc) laser diodes $\alpha_m(L_n) = -\ln(R_{uc})/L_n = \gamma_R/L_n$ differing only in lengths L_n. For these measurements, it is crucial to ensure that heat sink temperatures T_{HS} and corresponding device temperatures coincide. Therefore, the parameters have to be determined using the pulsed measurement with sufficiently short pulses at a sufficiently low repetition rate. The parameter extraction itself relies for the intrinsic optical parameters always on linear functions $Y = mX + b$ with slopes m and offsets b in order to gain accuracy by applying linear regression. Table 2.2. shows the procedure for parameter extraction in more detail. Based on Eq. (2.13), $1/\eta_i(T_{HS})$ and $\alpha(T_{HS})/(\gamma_R \eta_i(T_{HS}))$, i.e., α_i are extracted from offset and slope from $1/\eta_d$ versus L_n plots for different heat sink temperatures T_{HS}.

In a second step, the slope and offset from $\ln(j_{th}(T_{HS}))$ versus $1/L_n$ plots yield $\gamma_R/g_o(T_{HS})$ and $\ln[j_{tr}(T_{HS})] + \alpha_i(T_{HS})/g_o(T_{HS})$ based on Eq. (2.14). By using the already extracted parameter α_i, g_o and $\ln[j_{tr}(T_{HS})]$ can now be extracted. By using the equations for the coefficients, the characteristic temperatures T_α, T_η, T_{tr}, and T_g are finally computed by using the slopes of the corresponding $\ln(\chi)$ versus T_{HS} plots, where χ equals to α_i, η_i, j_{tr} and g_o, respectively.

The line series resistance ρ_S is extracted from measurements of the serial resistance for devices of various length which allows to eliminate the series resistance of the feeding circuitry. The voltage

$$U_o = \frac{hc}{e\lambda} \tag{2.23}$$

Table 2.2. Extraction of the intrinsic optical parameters from pulsed measured j_{th} and η_d at samples of various lengths L_n and heat sink temperatures T_{HS}

Input		Extracted Parameter	
X	Y	Slope	Offset
L_n	$1/\eta_d(T_{HS})$	$\frac{\alpha_i(T_{HS})}{\eta_i(T_{HS})\gamma_R}$	$\frac{1}{\eta_i(T_{HS})}$
$1/L_n$	$\ln(j_{th}(T_{HS}))$	$\frac{\gamma_R}{g_o(T_{HS})}$	$\ln[j_{tr}(T_{HS})] + \frac{\alpha_i(T_{HS})}{g_o(T_{HS})}$
T_m	$\ln(\alpha_i)$	T_α	
T_m	$-\ln(\eta_i)$	T_η	
T_m	$\ln(j_{tr})$	T_{tr}	
T_m	$-\ln(g_o)$	T_g	

can be at best extracted from the measured emission wavelength λ. Finally, the thermal resistance ρ_T which is significantly affected by the assembly of the laser, can be obtained by measuring p_{opt}, p_{el} and the emission wavelength λ at an operating point above threshold under pulsed and continuous-wave (cw) operation. The temperature difference between heat sink and active region under cw operation can be extracted from the difference between the emission wavelengths of pulsed and cw operation. The thermal resistance ρ_T is finally determined by using Eq. (2.18).

2.1.7. Optimizing High-Power Lasers

There is an increasing interest in applying high-power laser diodes for material processing. The increase of wall plug efficiency forms one of the most convincing arguments for their use. Within this context, the optimization of wall plug efficiency represents a generic task to maximize the wall plug efficiency but also to reduce the aging of the diodes.

Table 2.3. shows the parameters extracted for a high-power laser diode emitting at 808 nm and 940 nm. All temperatures are related to a heat sink temperature of 25°C.

TABLE 2.3. Extracted parameters, optimized external parameters result and several characteristic parameters after optimization for a high-power laser diode operating at 808 nm and 940 nm in the AlGaAs/GaAs material system

	808 nm	940 nm	
Extracted parameters			
$\alpha_i(T_{HS})$	0.02	0.01	1/nm
T_α	>300	300	K
$\eta_i(T_{HS})$	1.15	1.08	W/A
T_η	194	>500	K
$j_{tr}(T_{HS})$	0.1	0.13	A/mm
T_{tr}	350	85	K
$g_o(T_{HS})$	0.64	0.18	1/mm
T_g	90	>500	K
U_o	1.53	1.32	V
ρ_S	0.065	0.04	Ω mm
ρ_T	8.2	9.0	K mm/W
Optimization results			
ΔT	9.4	11.1	K
α_m	0.30	0.10	1/mm
j	1.57	2.01	A/mm
Related features			
ΔT_{th}	2.1	3.0	K
J_{th}	0.18	0.25	A/mm
P_{opt}	1.43	1.58	W/mm
η_W	55.5	56.2	%

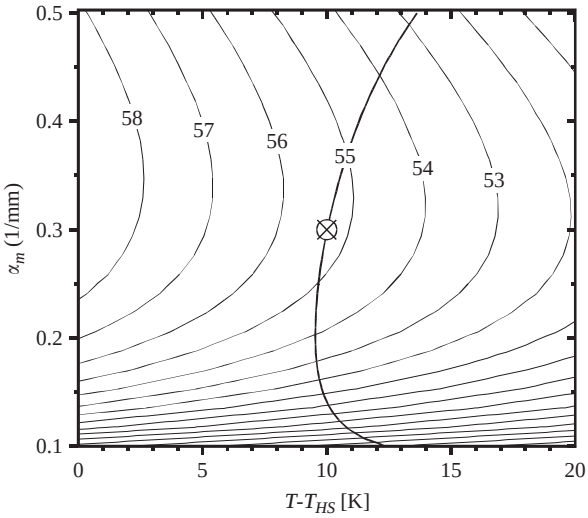

FIGURE 2.13. Contours of wall plug efficiency within the α_m -ΔT plane at constant line current density. The computed optimum and the curve of conserved power are included to illustrate the optimization result

Figure 2.13 shows contours of constant wall plug efficiency (unit: %), computed using Eq. (2.10), for a window in the α_m-ΔT plane close to the optimum. The thick solid line shows the trace of conserved power, i.e., the trace of realistic operating points in the α_m-ΔT plane. The optimum operation point computed using the Eq. (2.15) to (2.18) is also shown. It becomes obvious that the wall plug efficiency drops rapidly, if α_m drops, i.e., if the reflectance of the output facet becomes larger than its optimum value. A decreased reflectance, in contrast, seems to reduce the wall plug efficiency less. As a second result, better thermal connections of the heat sink leading to a lower temperature difference seem to result in a moderately increasing wall plug efficiency.

For a more detailed discussion, it is useful to examine the case of a front facet exhibiting the minimum reflectance accepted by the underlying application. For a front facet with e.g., $R = 3\%$, the optimized laser emits 8.47 W at a length of $L = 5.94$ mm. Starting from this point, the optical power can be further increased by increasing the device length and/or the applied current. Based on these results, it turns out to be useful to optimize the wall plug efficiency under the modified boundary conditions. Figure 2.14 shows the results of the wall plug efficiency and the emitted optical power as functions of the resonator length. Obviously, the wall plug efficiency drops rapidly if the length of resonator is smaller than the optimum length. But it becomes also apparent that the length of the resonator can be increased by another 5 mm at the expense of a moderate decrease $< 2\%$ of the wall plug efficiency. The reduction of the device length to 2 mm, in contrast, leads to a drastic reduction down to 10% of the wall plug efficiency. The wall

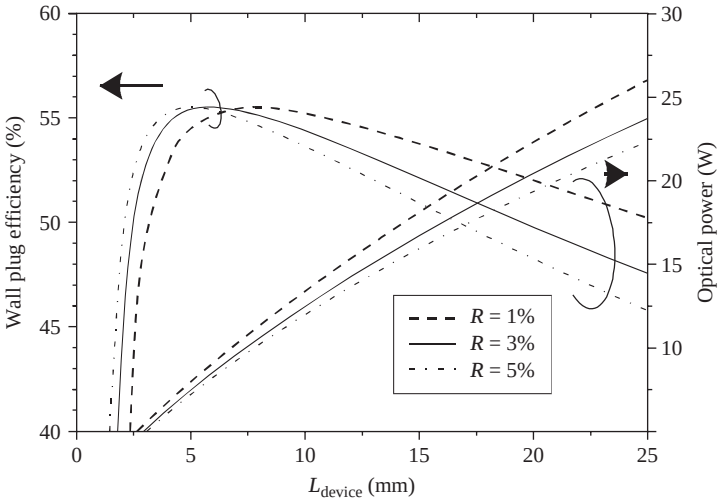

FIGURE 2.14. Optimized wall plug efficiency and corresponding output power as a function of the resonator length of the laser

plug efficiency versus $\log(L)$ drops nearly symmetrically close to its optimum, i.e., doubling and halving of the device length result approximately in the same reduction of the wall plug efficiency. Figure 2.14 shows also that the efficient use of the chip area with respect to the emitted optical power described by the figure of merit $\text{FOM} = [P(L)/P(L_{opt})]/[L/L_{opt}]$ drops, i.e., lengthy lasers use the chip area increasingly inefficient. The analysis of the second example in Table 2.3 shows, that a high-power laser diode emitting at 940 nm leads to similar results.

2.2. Manufacturing Technology

Martin Behringer

The most elementary semiconductor laser diode consists only of an optical active medium on a crystalline substrate having metal contacts for electrical current injection and two crystal facets to form an optical resonator. Such a device requires only few fabrication steps, namely, epitaxy, evaporation of the metal layer, cleaving the cavity facet, and cutting the chips out of the wafer. Sophisticated designs increasingly optimize the optical waveguiding as well as the light generation. For all devices, the fabrication starts with a crystalline substrate, the wafer, and continues with the epitaxial growth of the crystalline layers. Then, the surface is patterned into conducting and isolating areas. Finally, the end facets forming the resonator have to be manufactured. This section gives a brief description of state of the art epitaxial techniques and semiconductor technologies in respect of processing laser diodes.

2.2.1. MOVPE and MBE

A variety of epitaxial techniques for crystal growth have been developed during the last decades. For high-power laser diodes, epitaxial growth of III-V semiconductors, especially GaAs, plays a crucial role. Liquid phase epitaxy, growing the layers out of a melt, was used for a long time due to advantages of easy growing of very thick layers and parallel growth on many wafers at the same time. Today, crystalline growth out of the gas phase is preferred. Among these techniques, MOVPE and MBE are most commonly applied since they offer a good control of composition and thickness of the deposited layers and thus allow for the fabrication of complicated laser structures.

The principles of MOVPE (metal-organic vapor phase epitaxy) are often attributed to Manasevit et al., who worked during the 1960s [2.11, 2.12]. However, earlier activities in the field of MOVPE have been reported [2.13].

Figure 2.15 shows a typical MOVPE reactor. For growth, the substrates are moved from the loading position (a) to the growth position (b). During the growth, metal-organic precursors and hydrides are lead into a reactor, where they are decomposed and deposited on the heated substrate. This deposition usually takes place at temperatures in the range from 600°C to 800°C [2.14, 2.15]. Homogeneity, smoothness, and good electro-optical data form the main quality criteria of epitaxial layers which in turn determine performance parameters of the high-power lasers.

MOVPE has experienced a dramatic development during the last few years. The design of MOVPE reactors became more sophisticated, allowing better control of the composition and thickness (down to only a few monolayers) of the epitaxial layers. The list of improvements starts with the quality of the substrates (etch pit densities $<1{,}000\,\mathrm{cm}^{-2}$), continues with the homogeneity of the growth on the wafer, and ends with the reduction of contaminants in precursors used for growth. As a result, epitaxial layers of higher electron and hole mobility and less optical absorption at higher homogeneity and reproducibility became available. In parallel, a basic modeling of the MOVPE process has been established [2.14–2.17]. However, due to the complexity of these processes, the models suffer still from certain deficiencies. During the last years, in situ measurement allowed

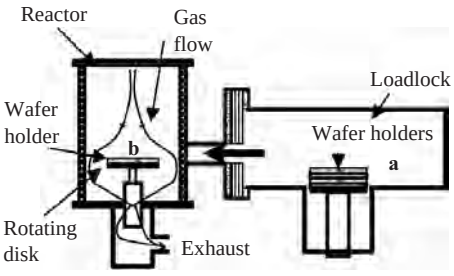

FIGURE 2.15. Schematic diagram of an MOVPE growth reactor and process

for an exact control of MOVPE parameters, such as the temperature of the wafers, the deposition rate and the composition of the deposited layers [2.18]. For the next years, these tools will enable the automated control of highly sophisticated MOVPE processes.

The option of large-scale production of highly advanced devices as well as their versatility are the main advantages of MOVPE over other epitaxial techniques. The use of hazardous materials and the complexity of the processes are its main disadvantages. However, today, industry learned to handle these processes well and therefore MOVPE is a widespread tool in III-V semiconductor industry. Due to the increasing size of the substrates and reactors, the cost of the devices could be significantly reduced. Whereas some years ago only a maximum of three 2-inch wafers could be processed at a time, current production reactors can process up to a hundred 2-inch wafers, or an equivalent number of 3- or 4-inch wafers [2.19, 2.20].

MBE (molecular-beam epitaxy) offers another option to fabricate similarly complicated devices. In contrast to MOVPE, MBE uses molecular beams of the different elements, without using a carrier gas or a precursor. Therefore, besides the good control over composition, doping, and layer thickness, MBE offers a further increase of the purity of the epitaxial layers. The main disadvantages of the MBE are the further increasing equipment cost and the interdependency between homogeneity of the layers and the homogeneity of the molecular beam which limits its use for large-scale production. Nevertheless, today both epitaxial growth techniques are well established. World records concerning efficiency, emitted power, device lifetime, and electro-optical characteristics have been achieved by using both techniques. Against this background, the decision in favor of the techniques is usually driven by secondary arguments like intellectual property and fabrication experience.

To summarize, today's high-power semiconductor lasers require:

- precise control of doping levels,
- precise control of layer composition,
- exact limitation of impurities in the layers,
- the ability to grow thin layers (fractions of a monolayer) and also thick layers up to a few micrometers,
- the ability to change composition and doping conditions during growth,
- high crystalline quality,
- good reproducibility and homogeneity.

Both growth techniques satisfy these requirements and are being used today.

2.2.2. Laser Processing

After epitaxial layer deposition, laser processing of the wafers can be carried out. Here the electrical contacts for current injection and the laser facets forming an optical cavity are realized. Figure 2.16 shows a typical broad area diode laser which consists of a substrate, epitaxial layers, grooves in the semiconductor

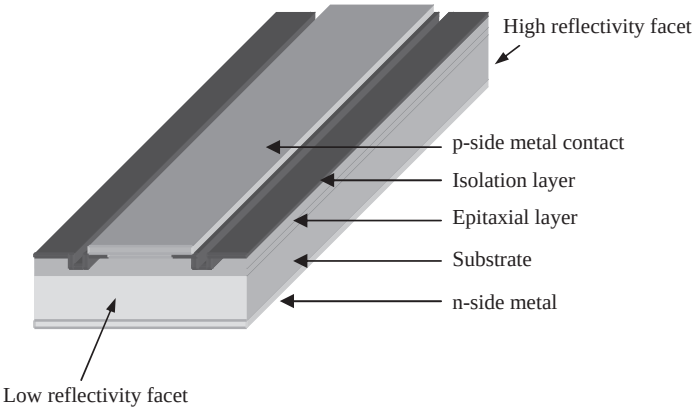

FIGURE 2.16. Typical design of a semiconductor diode laser

layers limiting the current spreading and preventing lasing perpendicular to the intended direction, isolating layers defining the region for current injection, metallic p- and n-contacts of the diode and the mirrors, forming a resonator. The following section describes the processing sequence from the semiconductor wafer to the final device.

In the first lithographic step, the active area is defined and transferred into the semiconductor epitaxial layers by using an etching step.

2.2.2.1. Photolithography and Patterning

As depicted in Fig. 2.17a, patterning of semiconductors starts with depositing a thin photo resist layer. This layer changes its physical and chemical characteristics when exposed to light. Illumination can be done either by direct writing with, e.g., a laser beam or an electron beam into the resist or by exposure with a master pattern. This master pattern can be 1:1 when contact of the wafer with the photo mask exists, or 1:4 or 1:5 when projection illumination is performed, using a reticle. Masks are, roughly spoken, transparent substrates with an opaque, usually metallic pattern that allows to illuminate certain areas and prevent illumination in other areas on the wafer. As shown in Fig. 2.17a, the photo mask is placed above the photoresist coated wafer and uniformly illuminated. Depending on the type of resist, the illuminated or the not illuminated fraction of the resist is washed out during the development process (see Fig. 2.17b). The resist pattern is transferred into the epitaxial layers by a subsequent etching process, e.g., wet chemical etching with an acid (see Fig. 2.17c), which ideally leaves regions covered by the resist unaffected.

Photoresists have to meet the following requirements:

- sensitivity at the wavelength used for lithography,
- chemical resistance against wet chemical solvents and dry chemical processes,
- complete stripping of the remaining resist at the end of patterning.

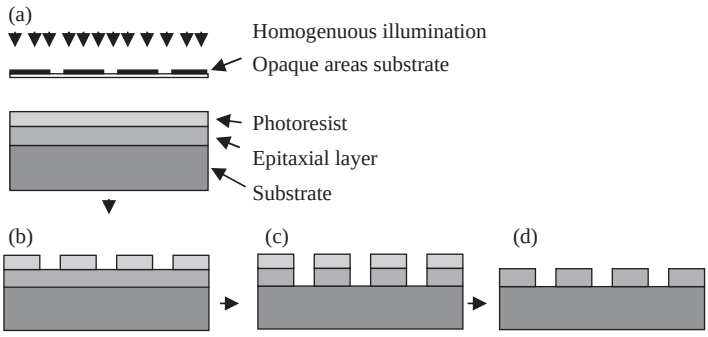

FIGURE 2.17. Photolithography: process sequence: (a) illumination of photoresist coated wafer, (b) developing and transfer of pattern into photoresist, (c) structuring of semiconductor layer, (d) removal of photoresist after patterning of wafer

The best photolithography process is selected by using the following arguments:

- shapes and sizes (dimensions) to be patterned,
- number of layers to be positioned on top of each other,
- required precision of overlay alignment needed for the device,
- wafer size and throughput in production.

Mask exposure offers the advantages of massive parallel processing, good pattern overlay, high resolution, high flexibility in defining patterns, high degree of automation, and almost unlimited possibility for rework on errors. It is one of the most important tools in semiconductor technologies today. Further information about this topic can be found in the literature [2.21–2.23].

Patterning can be done using wet chemical etching or dry chemical and/or physical etching techniques. Wet chemical etching represents a cost-effective, well established process for parallel processing of large areas and/or many wafers at a time. The solvents are chosen depending on the material. For wet chemical etching, also the crystal orientation can massively influence the etching speed and the vertical profile of the etched semiconductor surface. However, semiconductors of certain compositions cannot be etched by wet etching. Another possibility is etching from a gas phase or a plasma. For further details, see [2.24].

After etching, the resist is removed and the pattern that was once designed on the photomask has been transferred into the semiconductor (Fig. 2.17d). For defining the current injection area, an insulating layer is deposited onto the wafer surface, as can be seen in Fig. 2.18b.

2.2.2.2. Deposition of Dielectrics

Dielectrics are commonly deposited using plasma-enhanced chemical vapor deposition (PECVD), sputter deposition or evaporation. PECVD is also known as glow discharge chemical vapor deposition. It uses electron energy (plasma) as the activation method to enable deposition at low temperatures ($T < 500°C$) and

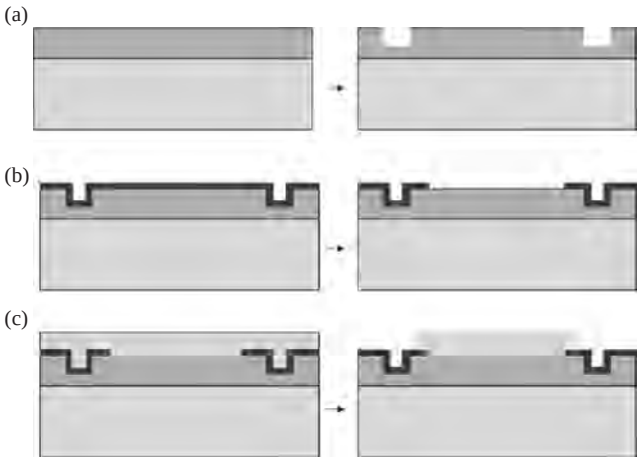

FIGURE 2.18. Process sequence in device technology: (a) structuring of semiconductor, (b) deposition of isolating layer and patterning, (c) metallization and patterning

at reasonable deposition rates. Supplying electrical power at a sufficiently high voltage to a gas at reduced pressures (<1.3 kPa), results in the breaking down of the gas and generates a glow discharge plasma consisting of electrons, ions and electronically excited species. The vapor reactants are ionized and dissociated by electron impact, hence generating chemically active ions and radicals that undergo the heterogeneous chemical reaction at or near the heated substrate surface and deposit the thin film. The versatility of PECVD has led to rapid growth, and this technology has become a very important processing method for the deposition of thin films and coatings for a wide range of applications, including dielectrics (e.g., SiO_2, Si_3N_4, AlN) for microelectronics and optoelectronics; refractory ceramic materials (e.g., SiC, TiN, TaN, Al_2O_3) used for hard coatings, protection against corrosion, oxidation, or as diffusion barriers; and metal films (e.g., W, Mo, Al, Au, Cu) for micro-electronics and for protective coatings. Compared to other deposition methods, PECVD has the following advantages:

- low operating temperature,
- fast processing time,
- good adhesion,
- controllability of the mechanical strain
- low pinhole density,
- very good step coverage,
- compatibility with pattern transfer processes, and
- adequate electrical properties.

In Fig. 2.19 a schematic of a PECVD rector is depicted. The wafers are carried on top of a carrier plate. Between the plate and an electrode, a plasma is generated and the dielectric is deposited onto the wafer.

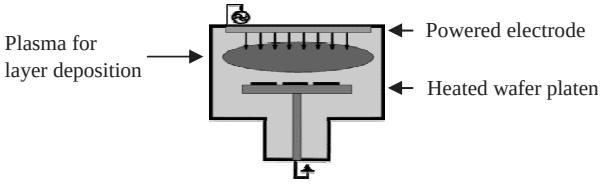

FIGURE 2.19. Schematic diagram of an PECVD reactor for dielectric layer deposition

After depositing the layer on the whole wafer area, the insulation is removed again from those areas of the chip, where the electrical current has to be injected, as shown in Fig. 2.18b. This can be achieved using photo techniques and etching in the same way as described above. Finally, a metal contact is deposited onto the wafer, as can be seen in Fig. 2.18c. The metal is deposited on the whole wafer again and removed after photolithographic definition of the contact structure and etching.

2.2.2.3. Metallization

The metal layer or layer stack is deposited either by evaporation or by sputtering. The metal area has to allow for:

- efficient current injection into the semiconductor,
- good current spreading over the whole contact area,
- good removal of waste heat, that is generated in the device and
- stable mechanical contact to the surrounding package.

Metal contacts are applied to both sides (p- and n-side) of the diode. Depending on the semiconductor and the doping different metals are chosen. The most commonly used materials on p-type doped GaAs are platinum (Pt), titanium (Ti), chromium (Cr), and gold (Au), on n-type doped GaAs germanium (Ge), titanium (Ti), nickel (Ni), and gold (Au) are used. For further details on what metal to chose and how to form ohmic or Schottky like contacts, please consult [2.25, 2.26].

2.2.3. Mirror Coating

For the definition of the laser resonator, the wafer is finally cleaved into bars whose facets are to be coated with dielectric mirrors. For realizing very precise facets, the crystalline structure of the semiconductor is of great advantage. As many compound semiconductors used for optoelectronics have a cubic lattice, the crystal can be cleaved in a way that the facets are perfectly parallel toward each other automatically. For mirror deposition, the cleaved bars are stacked on top of each other as shown in Fig. 2.20. The bars are stacked into special specimen holders for homogenous layer deposition. The design of the bar holders varies from about 50 to more than 500 bars. The special design of theses holders often is proprietary and is normally not published. The coatings are deposited in a vacuum

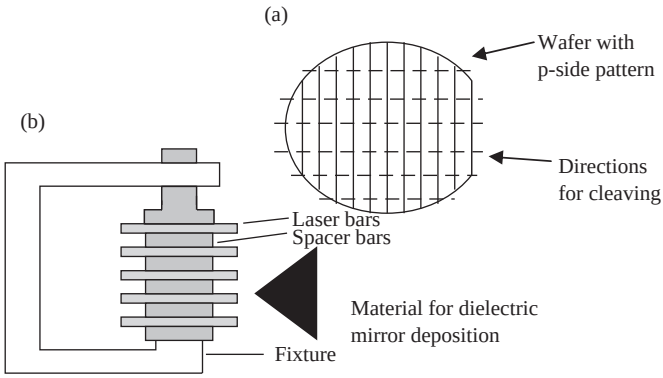

FIGURE 2.20. Mirror preparation: (a) cleaving a wafer and preparing laser bars, (b) stacking of laser bars for mirror deposition

system. While the mirror on the rear side has a reflectivity of almost 98% (high reflectivity side, HR), the front mirror allowing for light extraction has a much lower reflectivity (anti reflection side, AR). Therefore, the mirrors have to be deposited in subsequent fabrication steps.

The coatings for the facets have to provide the following properties:

- chemical and mechanical stability,
- good adhesion,
- low mechanical stress,
- high transparency at the laser wavelength and
- tunable optical properties.

These properties are crucial to obtain excellent behavior with respect to device lifetime and catastrophic optical mirror damage. Today, several different technologies for mirror processing are being used. The differences lie in the facet preparation and in the coating materials. The cleaving can be done either in vacuum or in normal atmosphere and the native oxide on the bars can be removed or transformed into some other material like AlN. For infrared high-power diode lasers, typical material combinations to obtain high reflectivity are: SiO/TiO or AlO and Si. Low reflectivity is normally realized using AlO or SiON. As the mirror has to sustain high optical field densities, only minimal deviations of this fabrication step can be accepted. Depending on what technology is being used, estimates on the costs for mirror deposition vary between $ 100 and only a few dollars per laser bar. For further information see [2.27–2.30].

2.2.4. Production and Processes

Today, high-power lasers are mainly made in the arsenic or phosphorus containing III/V-material system. In the future, power lasers based on (AlInGa)N will also be

available. Besides the pure manufacturability of lasers, costs play an increasingly important role. Production with little problems and high yield has to be considered when choosing the design of the laser chip, the technology of production, and the size of the individual unit. Therefore, after defining the requirements for the laser diode, the most simple design using the most simple processes that can fulfill the requirements for the laser diode sufficiently have to be chosen for a "production friendly" development. A less complicated design often results in lower rework rates; a well-established technology results in a higher uptime of machinery, and a smaller chip is more tolerant of manufacturing and handling errors than bigger laser bars. Also the degree of automation plays a crucial role in manufacturing costs. Normally, a higher degree of automation results in higher yield due to reduced mishandling, leading to lower production costs per unit on one side; but it results in higher costs of ownership on the other side. Therefore, depending on the volume, one has to choose the right equipment for production. A further factor is the lot size and the wafer size. Normally, not all areas of a semiconductor wafer can be used for diode laser production. For example, the outer parts or each wafer normally have higher defect densities and are consequently neglected in production. Therefore, it is more efficient to produce on a larger wafer scale if the handling does not cause additional new problems. One always has to consider:

- needs,
- volume,
- design,
- technologies available and
- expertise at hand

when designing the manufacturing process for an optoelectronic device.

2.3. Chip Characterization Methods and Measurements

Konstantin Boucke and Jens W. Tomm

2.3.1. Standard Characterization Methods

The reliable measurement of electrical, optical, and thermal properties is an essential tool during development and qualification of diode laser devices, but it is also necessary to supervise the quality of laser devices and mounting processes during production. Especially those parameters that are either of principal importance for the laser performance – such as output power and efficiency – or those that are indicators for reduced device reliability – such as burn-in and lifetime test results – have to be measured with high reproducibility and on a broad statistical basis, making it necessary to integrate these measurements into the production chain. This distinguishes these "standard" characterization methods from more advanced measurements which aim at a deeper understanding of diode laser devices in research and development.

2.3.1.1. Electro-Optical Characterization

The electro-optical characteristics determine the basic performance of the laser bar in terms of optical output power and electrical power consumption as a function of the driving current. Therefore, each laser bar undergoes an electro-optical characterization; some laser bar manufacturers perform an electro-optical characterization of the laser bars *before* mounting, and all manufacturers perform these measurements on the mounted bars before and after an initial device burn-in.

The results of a specific electro-optical characterization determines whether the measured laser bar meets its basic specifications, while the homogeneity and statistics of the characterization results over a number of identical bars yields information about the quality and stability of the production process. In many cases, specific problems in the production chain can be identified by analyzing abnormal electro-optical characterization results. Therefore, electro-optical characterization – although being a comparably simple measurement – is one of the most powerful tools for quality control in the production of laser bars.

For electro-optical characterization, the mounted laser bar is electrically contacted and connected to an appropriate cooling structure. For measuring the optical output power, typically an integrating sphere with attached photo diode is used instead of a thermal measuring head, because this measurement method is significantly faster and shows fewer deviations due to different beam divergence angles for uncollimated beams. Additionally, a spectrometer may be attached to the integrating sphere to simultaneously measure the spectral intensity distribution of the laser bar.

By increasing the driving current in a stepwise fashion from zero to a device-specific maximum current, the characteristic curves, optical power versus current $P_{opt}(I)$, voltage versus current $U(I)$, and peak wavelength versus current $\lambda_0(I)$ are measured, and the efficiency as a function of current is calculated.

$$\eta(I) = \frac{P_{opt}(I)}{I \cdot U(I)} \tag{2.24}$$

From the characteristic curves, further parameters are derived, such as the series resistance, the threshold current, and the slope efficiency:

$$\text{Series resistance } R_s[\Omega] \qquad R_S = dU(I)/dI \tag{2.25}$$

$$\text{Threshold current } I_{th}[\text{A}] \qquad I_{th} : d^2P_{opt}(I)/dI^2 = \max \tag{2.26}$$

$$\text{Slope efficiency } \eta_s[\text{W/A}] \qquad \eta_s = dP_{opt}(I)/dI \quad (I > I_{th}) \tag{2.27}$$

A detailed analysis of the characteristic curves gives information on the acceptable operation range and the load limits of the measured laser bar in conjunction with the chosen mounting technology and package type (Fig. 2.21). Ideally, the operating point of the laser bar should be close to the point of maximum efficiency. The pump current at which the maximum efficiency is reached can be adjusted, e.g., by changing the resonator length or the reflection coefficient of the front facet.

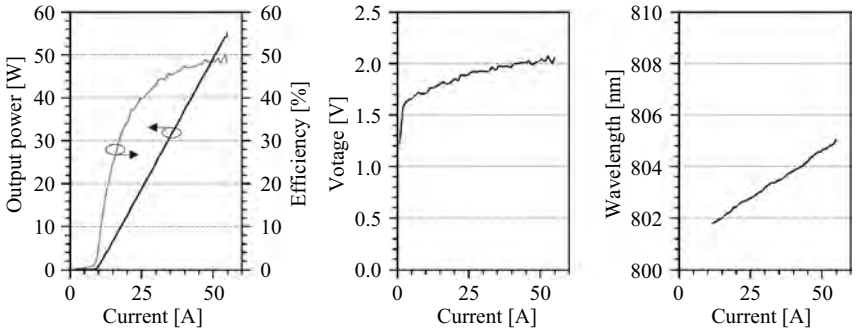

FIGURE 2.21. Sample characteristic curves, measured using an 808-nm broad-area laser bar with 19 emitters, 150 μm emitter width, 500 μm pitch

Critical for long-term operation of the laser bar is excessive thermal load. As a rule of thumb the operation temperature should not exceed 60°C, measured at the pn-junction. A measure for the temperature rise at the pn-junction is the emission wavelength of the laser. Typically, for GaAs laser devices the emission wavelength shifts with 0.27 to 0.29 nm/K toward longer wavelengths; therefore a temperature rise of 35°C from a base temperature of 25°C to 60°C corresponds to a wavelength shift of approximately 10 nm.

Increased operation temperatures lead to an increased threshold current and a reduced slope efficiency of the laser (see Chapter 2.1.3.), thus reducing the overall efficiency. This also takes place when the pump current is increased. Then the thermal degrading efficiency leads to the "thermal rollover" of the laser, indicated by a bowing of the P-I curve. Thermal rollover is a secure indicator of thermally overstressing the bar, resulting in a strongly reduced lifetime.

Different definitions are used for a quantitative determination C_{TRO} of the thermal rollover, either being based on the curvature of the P-I curve or the deviation of the P-I curve from an ideal straight line, measured at a given current level I_{TRO}:

$$C_{TRO} \sim \left.\frac{d^2P(I)}{dI^2}\right|_{I=I_{TRO}} \quad \text{or} \quad C_{TRO} \sim [\eta_S \cdot (I - I_{th}) - P(I)]_{I=I_{TRO}} \tag{2.28}$$

Besides the characteristic curves also the wavelength spectrum of the laser bar is of importance when judging the quality of a laser bar and it's packaging. A narrow Lorentzian-shaped spectrum without additional peaks is a positive indicator, while spectral broadening or a second peak in the spectrum can indicate defects or strong inhomogeneities in the chip material as well as packaging induced stress or defects. Typically, the spectral width of a state of the art broad area laser bar is between 1.5 and 2 nm (FWHM).

The following table summarizes typical electro-optical data of state of the art broad area laser bars with different emitter structures and different wavelengths.

Table 2.4. Typical electro-optical data for state of the art power laser bars

	808 nm 25 emitters	808 nm 19 emitters	980 nm 25 emitters
Cavity length	1.2 mm	1.2 mm	1.5 mm
Emitter width/pitch	200 µm/400 µm	150 µm/500 µm	200 µm/400 µm
Fill factor	50%	30%	50%
Max. current	65 A	50 A	70 A
Max. output power	60 W	50 W	55 W
Max. voltage	2.0 V	2.1 V	1.8 V
Max. efficiency	55%	55%	65%
Threshold current	14 A	9 A	12 A
Slope efficiency	1.15 W/A	1.15 W/A	1.05 W/A
Fast axis divergency[1]	60°	60°	65°
Slow axis divergency[1]	8°	8°	8°
Spectral width (FWHM)	2 nm	2 nm	2.5 nm
Degree of polarisation	>90%	>90%	>95%

The thermal operation conditions of the laser bar are mainly governed by the thermal resistance R_{th} of the laser package,

$$R_{th} = \frac{\Delta T}{P_{therm}} \tag{2.29}$$

where ΔT is the temperature rise in the pn-junction caused by the thermal power P_{therm} dissipated by the laser bar during operation (see Chapter 3.3). The thermal resistance is a function of the laser bar structure as well as of the package type and structure. Since the thermal resistance – and the resulting operating temperature as a function of the current – is the main factor limiting the average output power of the laser bar, and because a typically high values of the thermal resistance are a good indicator for failures in the packaging process, the measurement of the thermal resistance is also of great importance for design and diagnostic purposes.

A very accurate and easy method to obtain the thermal resistance makes use of the temperature dependence of the laser wavelength to measure the temperature rise in the pn-junction. To determine the precise thermal wavelength drift factor $\Delta\lambda_{th} = d\lambda/dT$ of a given laser structure, the emission wavelength of the laser has to be measured at different temperatures and in the "power-free" limit, $P_{therm} = 0$, meaning with very short pulse durations (<1 µs) and a low duty cycle (<0.1%). With knowledge of the drift factor $\Delta\lambda_{th}$ and the emission wavelength in the "power-free" limit, $\lambda(P_{therm} = 0)$, the thermal resistance can be directly calculated

[1] Full angle, 95% enclosed power.

from the electro-optical characterization data:

$$P_{therm} = U(I) \cdot I - P_{opt},$$
$$\Delta T(P_{therm}) = \frac{\lambda(P_{therm}) - \lambda(P_{therm} = 0)}{\Delta\lambda_{th}}$$
$$\Rightarrow R_{th} = \frac{\Delta T(P_{therm})}{P_{therm}} \tag{2.30}$$

2.3.1.2. Far-Field and Beam Divergence Angles

For the proper design of optics, such as fast-axis and slow-axis collimators (see Chapter 4.2), the knowledge of the angular beam distribution, equivalent to the far-field of the laser bar, is required. In fast-axis, perpendicular to the epitaxial layers of the laser, the laser beam can be well approximated by a Gaussian beam: The thickness of the waveguide layers is small enough to support only the fundamental mode. An important information for the optics design is the beam divergence angle, because it dictates the required numerical aperture of the collimation optics and yields the beam width in fast direction after collimation, as a function of the focal length of the optics.

In slow-axis direction, the beam profile is dominated by the presence of higher-order modes, and the detailed profile depends on the laser structure and type. However, also in slow-axis typically only the beam divergence angle is required as a design parameter.

The measurement of the far-field intensity distribution of a laser bar is performed by rotating the bar around its vertical and horizontal axes, with the turnpoint in the center of the front facet. The intensity as a function of the angular position is detected by a photo diode behind a pinhole. To avoid distortions of the measured far-field, the distance between laser bar and the pinhole has to be large enough: Due to the lateral extension of the laser bar in slow-axis direction, the detector receives beams under different angles from the left-most and right-most emitters of the bar, resulting in a limited angular resolution of the measurement (Fig. 2.22). As seen from the detector, in the center position, the angle between the edges of the laser bar is given by

$$\tan\left(\frac{\Delta\alpha}{2}\right) = \frac{b}{2d} \quad \Rightarrow \quad \Delta\alpha = 2\arctan\left(\frac{b}{2d}\right) \tag{2.31}$$

For all other detector positions on a circle with radius d the angle $\Delta\alpha$ is smaller. For a 10 mm bar, the calculation shows that a distance d of approximate 1 m is required to achieve an angular resolution of $\Delta\alpha < 0.5°$.

By rotating the laser bar around fast and slow axes, a two-dimensional scan of the far-field intensity distribution $I_{FF}(\varphi, \theta)$ can be generated. Under the assumption that the fast-axis and slow-axis are precisely aligned to the rotational axes of the measurement set-up, the axes are independent of each other and it is sufficient to

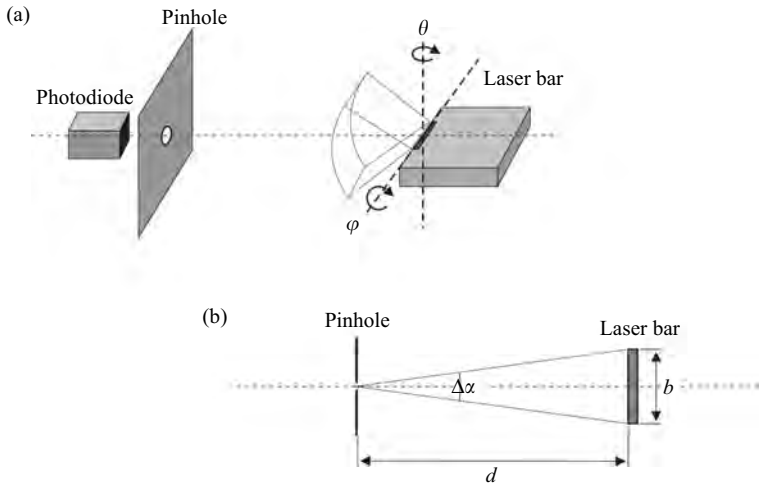

FIGURE 2.22. (a) Schematic set-up for the far-field measurement of a laser bar. (b) Determination of the minimum required distance between laser bar and detector

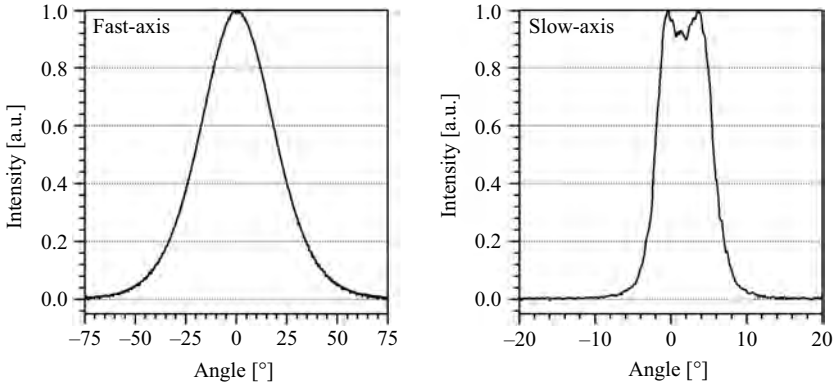

FIGURE 2.23. Fast-axis and slow-axis far-field intensity distributions of a standard broad area laser bar

measure only one-dimensional profiles along fast and slow axes (Fig. 2.23). From these profiles, the fast- and slow-axis divergence angles can be calculated.

For the divergence angles different definitions are in use: The definition of the beam radius and divergence angle by the decrease of the intensity to $1/e^2$ of the maximum intensity is derived from the theory of Gaussian beams. A general parameter to characterize the width of a distribution is the "full width at half-maximum" (FWHM) criterion. Finally, motivated by the practical need of achieving a certain transmission efficiency through optics with limited aperture,

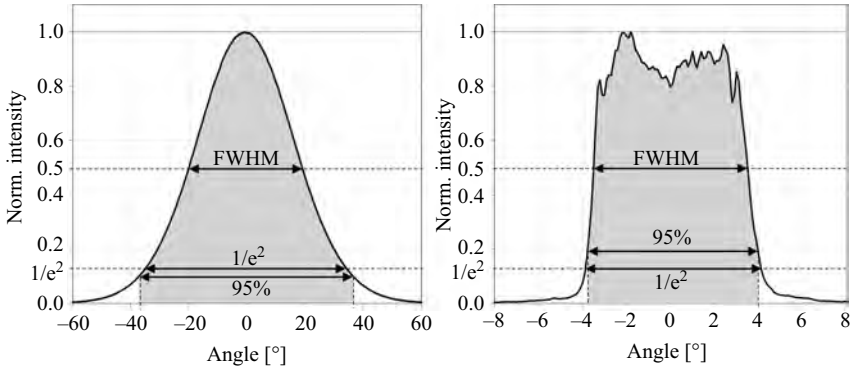

FIGURE 2.24. Determination of divergence angles according to different definitions

the criterion of 95% power inclusion is defined.[2] Figure 2.24 shows the different definitions for the divergence angle with typical fast-axis and slow-axis far-field intensity distributions.

In fast-axis, all commercially available high-power diode lasers show an approximately Gaussian far-field intensity distribution.[3] Varying values of the divergence angle result from differences in the epitaxial layer structure of the laser: so-called LOC (large-optical-cavity) structures are now widely used to reduce the fast-axis divergence angle. The reduction of the fast-axis divergence angle is important in order to enable the use of fast-axis collimation optics with smaller numerical aperture, being less expensive and less sensitive against aberrations and misalignment. During recent years, optimized laser designs led to a reduction of the fast-axis divergence angle from 80° down to 60° or even 45° for some laser types (see Fig. 2.25).

Also, in slow-axis different far-field patterns can be observed, depending on the lateral laser structure. Standard broad area lasers show a top-hat-like far-field, while especially the so-called "multi-stripe" geometry tends to a double-lobed far-field. By optimization of the laser structure, material parameters, and processing, a reduction of the divergence angle has also been achieved in slow-axis . However, while the reduction of fast-axis divergence mainly serves the simplification of the collimation optics, the divergence reduction in slow-axis directly indicates

[2] As a matter of fact, this criterion is not based on "enclosed power" but on "enclosed linear power density," because the two-dimensional, angular intensity distribution is only integrated along one axis (fast-axis or slow-axis) to obtain the divergence angle for fast-axis or slow-axis. Combined for both axes, this criterion corresponds to a rectangular aperture with dimensions in fast- and slow-axis chosen appropriately to transmit $(95\%)^2 \cong 90\%$ of the total power.

[3] Slight deviations from the Gaussian shape arise from the fact that the zero-order mode of a planar waveguide is not precisely a Gauss mode.

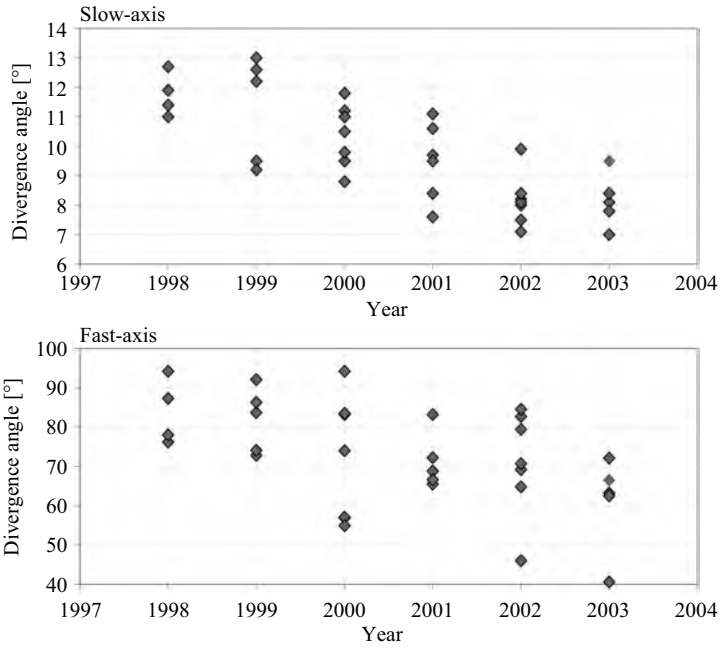

FIGURE 2.25. Development of the fast-axis and slow-axis divergence angles (full angle, 95% enclosed power) during the last years, according to measurements on commercial and R& D laser bars of different types and from different sources. In spite of the large variation of the values between different laser bar types, a general trend to reduced divergence angles in both axes can be seen (Measurements performed at the Fraunhofer Institute for Laser Technology)

an improvement in beam quality when comparing laser structures with the same stripe width.

While the fast-axis far-field typically shows no dependence on the operation current when above the threshold, in slow-axis most high-power diode lasers show some increase of the divergence angle with increasing current (Fig. 2.26). Different mechanisms contribute to this effect: The increased current leads to a stronger current spreading and higher temperature gradients between the center and the edges of each emitter, resulting in a widening of the far-field pattern. Additionally, at higher operation currents, the filamentation of the intensity distribution is amplified, reducing the beam quality and thus enlarging the divergence angle.

2.3.2. Advanced Characterization

This section deals with several analytical tools and techniques which can be applied to "cm-bars" *additionally* in order to learn more details about their performance and reliability limits as well as to identify weak points of the device design or the

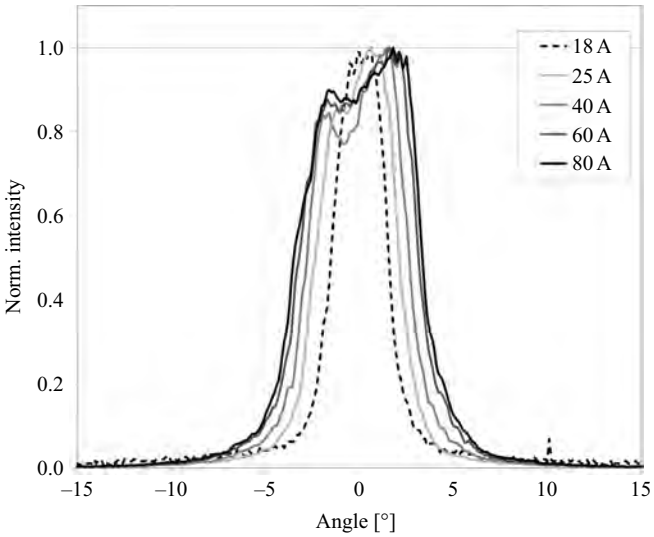

FIGURE 2.26. Change of the slow-axis far-field intensity distribution with increased operation current, measured on an 808-nm laser bar

technology applied. The application of these techniques offers additional chances to locate sources of degradation and for obtaining insight into the microscopic processes that affect the devices during operation.

2.3.2.1. "By-Emitter" Analysis of Standard Parameters

Emission wavelength, power, line width, and thermal tuning rate are standard device parameters (see section 2.3.1). In some cases it is useful to measure these parameters separately for each single emitter of a "cm-bar," since knowledge of standard parameters on a "by-emitter-scale" provides information about bar uniformity. Thus "by-emitter analysis" allows us to identify defective emitters, but it also provides information about packaging-induced stresses and defects [2.31, 2.32]. Figure 2.27 shows the emission pattern of a "cm-bar" array consisting of 19 emitters at 22°C and 58.5°C heat sink temperature. The pattern is detected by a CCD-camera mounted to the exit of a monochromator. As expected for increasing temperature, the emission wavelength is shifted toward the infrared according to the temperature dependence of the energetically lowest quantum-well transition, which is responsible for lasing. In addition, the wavelength homogeneity across the array is substantially changed. The "bow-like" behavior (top) is replaced by an almost uniform distribution (bottom). From such pattern one can easily determine "thermal" tuning rates for single emitters which differ substantially. These tuning rates are influenced by a variety of effects, among others (a) local temperature, (b) packaging-induced strain, and (c) all kinds of non-homogeneities, which are built into the device during wafer fabrication or epitaxy.

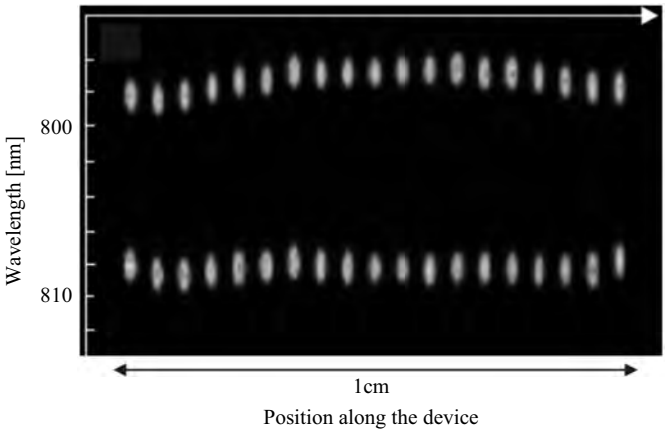

FIGURE 2.27. Emission pattern of a "cm-bar" array consisting of 19 emitters at 22°C (top line of emission spots) and 58.5°C (bottom line of emission spots) base heat sink temperature measured by a thermistor that is located about 3 mm off the actively cooled heat sink of the array. This pattern is detected by a CCD-camera

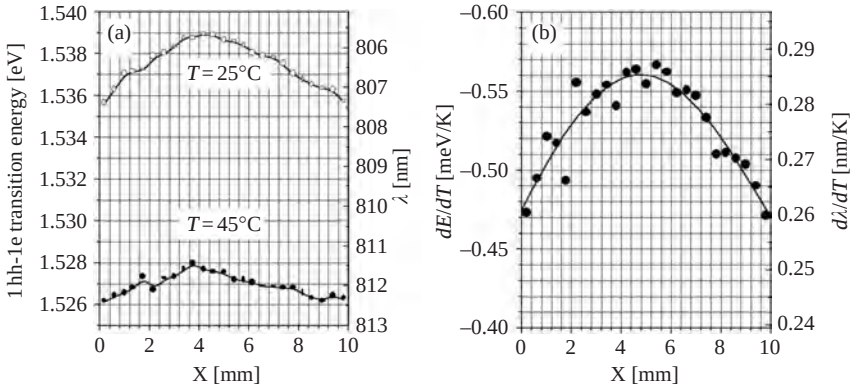

FIGURE 2.28. (a) Position of the energetically lowest optical transition in the QW versus local position along the "cm-bar" array consisting of 25 emitters. Measuring temperatures are 25 (open circles) and 45°C (full circles). Thermal tuning rate of the lasing transition versus local position along a "cm-bar" array consisting of 25 emitters. (b) The result presented in this figure is determined from the data shown in Fig. 2.28(a) by subtracting the positions for both temperatures and dividing them by the temperature difference

In order to eliminate the uncertainty of the temperature distribution within the device thermal tuning rates are determined by Fourier-transform (FT) photocurrent spectroscopy (PC) see [2.32, 2.33]. In Fig. 2.28a the energetically lowest optical transition in the quantum well is plotted versus local position along the device. From these raw data we determine "by-emitter" tuning rates (compare Fig. 2.28b).

These "by-emitter" tuning rates are free of any thermal non-uniformity effects and reflect the genuine change of the semiconductor band structure along the array, namely, the modification of the packaging-induced stress along the bar for two different temperatures. Now we recall our earlier experimental finding that the packaging-induced strain in In-packaged "cm-bar" arrays vanishes toward the bar edges, i.e., at $x = 0$ and 10 mm [2.32]. Thus we can use these locations as "zero-reference" and are now able to give absolute numbers for the packaging-induced strain. Using the strain sensitivity of -2.1 eV (cf. [2.34]), we obtain from the 3.1- and 1.8-meV "bowings" for 25°C and 45°C (see Fig. 2.28b), center-of-bar-strains of about -0.15% and -0.09% , respectively. In other words, in our example, about 40% of the packaging-induced strain vanishes when the device is heated up by 20°C. It is possible to take benefit from the knowledge about the packaging-induced strain and to separate the tuning rates into two parts, namely, into the pure *thermal* tuning contribution ($-0.48\,\mathrm{meVK^{-1}}$) and *mechanical pressure* tuning contribution of $-0.56\,\mathrm{meVK^{-1}} - (-0.48\,\mathrm{meVK^{-1}}) = -0.08\,\mathrm{meVK^{-1}}$. The latter one is, of course *indirectly*, also a thermal one, because the mechanical deformation is caused by the temperature increase. Nevertheless, we can state that about 15% of the "thermal tuning rate" of the central emitters in this "cm-bar" array is actually caused by pressure tuning. The use of "by-emitter" tuning rates (see [2.34]), allows for the statement of more accurate local temperatures along arrays. Thus a systematic error of about 15% that is potentially involved in temperature data that are derived from the emission wavelength by using one constant "integral" tuning rate can be ruled out by the "by-emitter" approach. The investigation of the polarization of the device emission on a by-emitter scale also offers useful information.

Figure 2.29 shows electroluminescence scans along a 25 emitter InGaAlAs-"cm-bar." Figure 2.30 gives the spatial variation of the degree of polarization of Fig. 2.29. The degree of polarization provides *qualitative* information about the spatial variation of the packaging-induced strain. The increase toward the

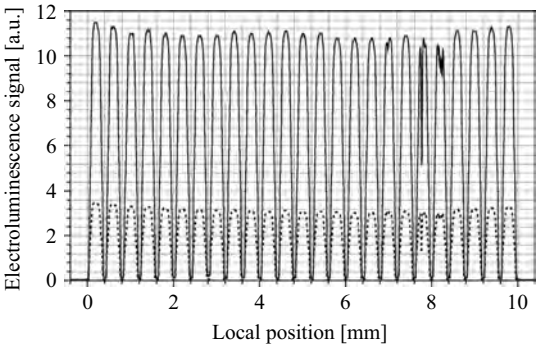

FIGURE 2.29. Electroluminescence scans along an InGaAlAs-"cm-bar." The operation current is 0.5 A, i.e., about 5% of the laser threshold for this kind of devices. By using a polarization filter TE- (full line) and TM-scans (dotted line) are monitored separately

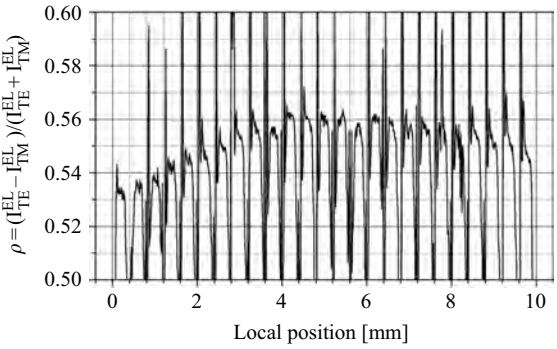

FIGURE 2.30. Degree of polarization (ρ) of the electroluminescence versus local position. The result presented in this figure is determined from the data shown in Fig. 2.29

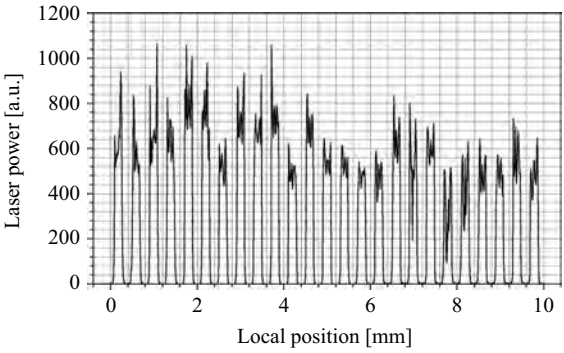

FIGURE 2.31. Laser emission at I = 20 A along the same InGaAlAs-"cm-bar," which data are already presented in Fig. 2.29 and Fig. 2.30

center of the bar is caused by decreased TM-emission due to the increased split between heavy-hole and light-hole-valence-band in the quantum well of the laser structure. This leads to a reduced hole population of states in the light-hole band. Thus Fig. 2.30 *qualitatively* confirms the quantitative result that is presented in Fig. 2.27 and Fig. 2.28. Consideration of the electroluminescence pattern without using of the parameter "polarization" allows at least the identification of defective emitters at 7.0, 7.8, and 8.2 mm in Fig. 2.29. Information about laser power for this particular 25 emitter containing InGaAlAs-"cm-bar" completes our discussion.

Figure 2.31 shows that the emitters at 7.8 and 8.2 mm, which are affected by dark-line defects, show poorer lasing, whereas the emitter at 7.0 mm shows surprisingly more emission than other emitters which are nominally "defect-free," e.g., the emitter at 9 mm. This apparent contradiction becomes clarified if one takes into account that the electroluminescence pattern provides information about the region about one diffusion length deep into the device (i.e., several microns from the mirror), whereas the lasing is affected by device properties along the whole

cavity length. Furthermore, for electroluminescence ($I = 0.5$ A) an almost uniform thermal distribution can be presumed, whereas for the case of lasing ($I = 20$ A), this is definitely not guaranteed any longer. Furthermore, power redistributions between the emitters represent an important issue.

It is noteworthy that only the "by-emitter" parameters, which are based on *spectral* information (see Fig. 2.28), are genuine parameters that refer nearly exclusively to individual emitter properties. For those parameters that rely on *intensities* (see Fig. 2.29 and Fig. 2.30) it must be conceded that non-uniform current distributions through the emitters, which are connected all in parallel, represent an additional parameter of uncertainty. This limitation, however, does not prohibit the conclusion that by-emitter analysis, i.e., the measurement of local device parameters along a device, represents a useful tool for identifying defective emitters as well as for the quantification of packaging-induced stresses.

2.3.2.2. Facet Temperatures: Raman Analysis

The micro-Raman technique is an established spectroscopic method for *surface temperature* measurements [2.35–2.39]. Thus micro-Raman represents a complementary technique to the measurement of the *averaged cavity temperature* from the laser emission wavelength. Since the laser facets are part of the laser cavity, their temperature is determined by both, the averaged cavity temperature plus the temperature increase caused by extra heat sources at the surface. Thus facet temperatures are higher than averaged bulk temperatures. The facet temperature measurements presented here are performed by micro-Raman spectroscopy. A DILOR x-y-Raman-spectrometer equipped with a microscope (spatial resolution of about 1 μm corresponds to the waveguide thickness) and a liquid-Nitrogen-cooled CCD-camera that allows for synchronous signal pick-up of the Stokes and anti-Stokes GaAs-or AlAs-like TO-phonon peaks generated at the device waveguide serves as a surface-temperature micro-probe. As excitation source we use the 514.5-nm line of Ar^+-ion laser creating a temperature probe with a depth-resolution of about 100 nm. Temperature calibration is done quite straightforwardly by measurements with reference devices that were heated upto more than 300°C. The device itself is mounted on a temperature-stabilized heat sink (typically stabilized at 25°C) that allows for active alignment of the device waveguide with respect to the microscope objective by using x-y-z-piezo translation stages.

We measure surface temperatures for both pulsed and cw operation. In case of pulsed operation we apply 5 μs pulses at repetition rates between 10 and 50 kHz. In this case the Ar^+-ion laser is modulated by an electro-optical modulator triggered by the laser pulse power supply. Such pulsed μ-Raman facet temperature measurements are described in detail by Kranz et al. [2.38].

Information on the local temperature in the surface layer was derived in two ways; from the ratio of the anti-Stokes and Stokes line intensities and – independently – from the spectral positions of those lines. Test experiments revealed that the lattice heating caused by the cw excitation laser does not exceed 10 degrees

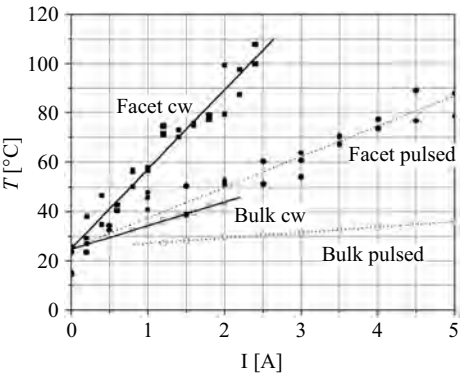

FIGURE 2.32. Facet (full symbols) and bulk (open symbols) temperatures in a 808-nm InAlGaAs/AlGaAs/GaAs high-power diode laser "single-chip" versus operation current. Squares mark cw data, whereas circles represent data obtained in pulsed operation. The heat sink temperature is stabilized at 25°C

if the excitation power is kept below 850 μW. Furthermore, we always subtract from the actual spectrum a spectrum that is monitored without the presence of excitation laser light. The experimental setup as well as methodology has been described more in detail in [2.39].

Figure 2.32 shows facet temperatures determined by micro-Raman spectroscopy and bulk temperatures derived from the emission wavelength of an 808 nm emitting InAlGaAs high-power diode laser "single-chip" device versus operation current for cw-operation as well as for pulsed excitation. For the bulk temperatures the expected result, a significant reduction of the thermal load, is visible when switching from cw to pulsed operation. This reduction is also the main motivation for using this operation mode in our experiments. At 2 A the cw facet temperature amounts to about 90°C, i.e., well below the 120–140°C that are considered critical for facets of lasers made of the AlGaAs-system (cf. [2.37]). Figure 2.32 demonstrates the significant reduction of both bulk and facet temperatures when switching from cw to pulsed. The reduction of the facet overheating (factor of about 2) is significantly weaker than the bulk temperature reduction (factor of about 5). This effect is understood by taking into account the different thermal relaxation behavior of facet and bulk, cf. also [2.38]. Deeper insight into the quantities, however, requires accurate thermal modeling (see [2.40]). The discussed effect is mainly used to reduce the bulk heating contribution to the facet temperature as well as for being able to perform measurements at operation currents higher than the nominal ones.

Results from 940-nm-emitting high-power "single chip" devices with and without current blocking layer at the front facet show interesting differences (see also [2.41]). Threshold and slope efficiency for both are found to be almost similar. This is not surprising since a 30 μm current blocking layer at 2 mm long laser cavity should not substantially affect their amplification properties. A striking

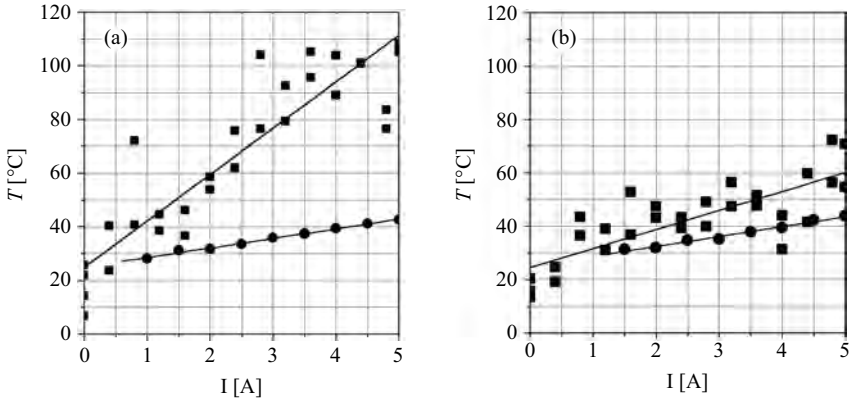

FIGURE 2.33. (a) Facet (full squares) and averaged bulk (full circles) temperatures for a 940 nm InGaAs/AlGaAs/GaAs high-power "single-chip" lasers without current blocking layer versus cw operation current. (b) Facet (full squares) and averaged bulk (full circles) temperatures for a 940 nm InGaAs/AlGaAs/GaAs high-power "single-chip" lasers with a 30 μm current blocking layer versus cw operation current

difference, however, is seen for the facet temperatures, where a reduction of the facet overheating by a factor of 4 is observed (see Fig. 2.33). Reproducibility tests with other sets of lasers provide reductions by a factor between 3 and 4. Regardless of this impressive evidence of the success of a technological measure another very important conclusion may be drawn from this experiment. Since the optical load for the facets of both lasers is almost similar it is clear that the *facet heating is not caused by reabsorption* of laser light. This important finding is in excellent agreement with former results obtained by other authors for QW lasers (cf. [2.37] and [2.42]). Facet heating by surface currents is considered a likely explanation.

2.4. Broad Area Emitters and Arrays

Martin Behringer

In the previous chapters, it was mentioned that diode lasers for direct laser processing mainly convince through the excellent wall plug efficiencies (up to 70% in comparison to 5% for lamp pumped solid-state lasers [SSL], 10% for diode pumped SSL, and 20% for disk laser). High optical power is always correlated with:

- high operating current,
- high optical power load at the chip end facets,
- high heat load (also for highly efficient devices).

The successful operation and required stability against the induced stress requires consideration of a number of design aspects.

- As a rule of thumb, it is necessary to apply a current of ≈1 A to obtain an optical output of 1 W (at a wavelength of ≈1 μm). For laser bars emitting 50 W this results in a total electric load of ≈50 A. Therefore, large contact areas and a large pn-junction area for the optical emission must be applied to minimize the local current densities.
- The increase of wall plug efficiency represents the best way to reduce the heat load. Current efforts aim to increase this figure from 40% (standard a few years ago) upto 80%. Besides these attempts, it is still necessary to dissipate the generated heat through the contact area more efficiently, e.g., by using larger heat transfer areas.
- Minimizing electrical losses, especially at high current densities, requires low series resistances, which can be reduced by enlarging the contacts, increasing the doping levels, and improving the electron and hole mobility inside the epitaxial layers.
- Efficient emission and low scattering or absorption losses can be achieved by optimizing the quality of the epitaxial layers and by improving the waveguide and quantum well design.
- Catastrophic optical mirror damage (COMD) can be avoided by using a large optical cavity (LOC) in order to reduce the local optical power density at the end facets.

Current high-power diode lasers consider all these aspects. Since the requirements are partly contradictory, it is impossible to fulfill them all at the same time. Nevertheless, modern high-power diode lasers exhibit the following typical characteristics: long resonator, wide contacts, and large optical cavity, as can be seen in Fig. 2.34.

Besides the operation conditions for the diode itself, the emission pattern has to be considered, when the radiated power needs to be redirected using systems of optical elements.

In the following section, the design of today's high-power diode lasers is briefly discussed and typical data are presented.

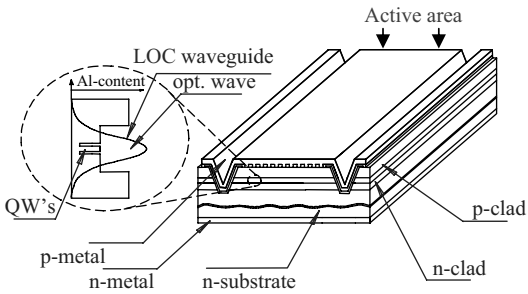

FIGURE 2.34. Schematic of a diode laser

2.4.1. Design and Material Parameters

As mentioned above, it is desirable to increase the width of the optical wave over a larger area. Some designs confine the optical wave in horizontal direction by incorporating a sharp index step using layers with different refractive indices. Some designs increase the loss for higher-order modes and thus support the desired optical wave in comparison to undesired modes. Large optical cavities (LOC) were first described by Garbusov et al. [2.43], who used a 1.2-μm-wide AlGaAs (40% aluminum) waveguide and AlGaAs (60% aluminum) cladding layers. Commercially available high-power diode lasers today expand the wave's height to 1 μm to 2 μm and upto 400 μm in the horizontal direction per emitter. New attempts to widen the optical wave further use a kind of photonic band gap structure. With this, the fundamental mode is spread out over a height of upto 20 μm, resulting in both, a low optical intensity at the mirror facet and a narrow far-field pattern in vertical direction. In Fig. 2.34 a typical emitter for high-power emission is depicted. It shows a wide contact, a long resonator, and a high epitaxial layer structure for a large optical waveguide. The main parameters for the design are summarized in section 2.1.

2.4.2. Electric and Optical Characteristics

2.4.2.1. PI Characteristics and Wall Plug Efficiency

The most important advantages for the application of high-power diode lasers include the high wall plug efficiency and the direct tunability of the output power by controlling the electric current through the device. Figure 2.35 shows an optical power versus current and operating voltage versus current characteristic of a high-power laser emitting at 940 nm. Upto the threshold current of $I_{th} \approx 10$ A, only spontaneously emitted photons, i.e., at very low optical power, can be observed. Above the threshold, the output power increases linearly with the driving current. The slope efficiency depends on internal quantum efficiency, the reflectivities of rear and front facets and absorption within the semiconductor material and on the frequency of the emitted photons. Here, the slope efficiency is $\eta \approx 1.2$ W/A for currents between 11 A and 80 A.

When the current is switched on, the voltage over the pn-junction increases rapidly to a value of U ≈ 1.4 V, which corresponds to a photon energy of ≈1.4 eV. Above this value, the voltage increases slowly with increasing current due to the series resistance. Due to the low series resistances, this increase is small in state-of-the-art high-power laser diodes. As a second consequence of the low series resistances, the wall plug efficiencies attain typically maximum values of 50% to 60%. It becomes obvious from the left part of Fig. 2.35 that the wall plug efficiency of the examined laser is <1% below threshold and about 65% at an operating current $I_{op} \approx 80$ A (80 W). At very high operating currents ($I_{op} > 100$ A), the wall plug efficiency drops slowly due to the series resistance and resulting heat

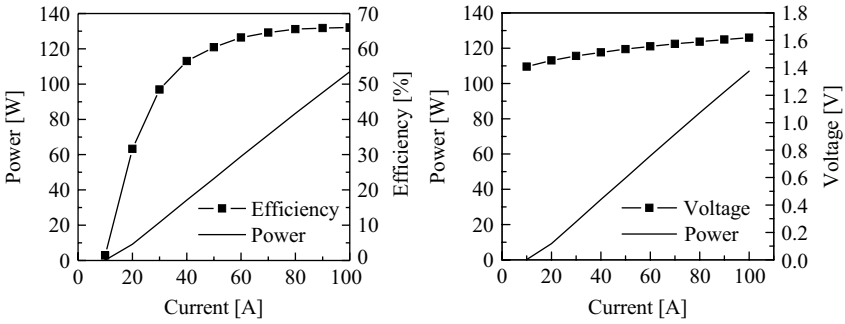

FIGURE 2.35. Light-current; efficiency-current (left) and light-current; voltage-current (right) diagram of a diode laser bar for 940-nm emission

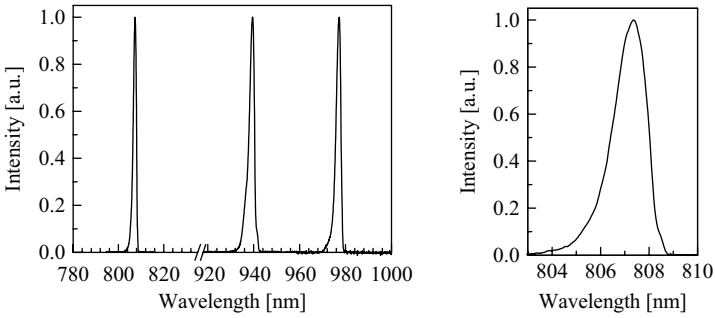

FIGURE 2.36. Emission spectrum of 808-, 940-, and 980-nm 1-cm laser bar

generation in the device. Typical values for state of the art high-power diode lasers in the different spectral regions are given in section 2.3.1.

2.4.2.2. Emission Spectrum

Wavelength multiplexing (cf. Chapter 4.3.2) represents a promising technology to increase the local power density for direct laser processing. The ability to narrow the emission spectrum and to actively determine the wavelength of a fabricated laser structure are two necessary conditions for the use of this technique. Figure 2.36 depicts the spectra of diode lasers emitting in the 808-, 940-, and 980-nm-wavelength range.

All spectra were measured using cw operation on bars which were mounted on actively cooled heat sinks. Obviously, all devices emitted within a spectral window of $\Delta\lambda < 5$ nm. The zoomed part of the spectra demonstrate that the full width at half-maximum (FWHM) is typically 2 to 2.5 nm irrespective of the emission wavelength. As has already been pointed out, the homogeneity over the wafer production as well as wafer-to-wafer reproducibility are indispensable for successful control of the wavelength on a commercial basis. Figure 2.37 shows the measured peak wavelengths of 600 diodes located on two 4-inch wafers out of a common

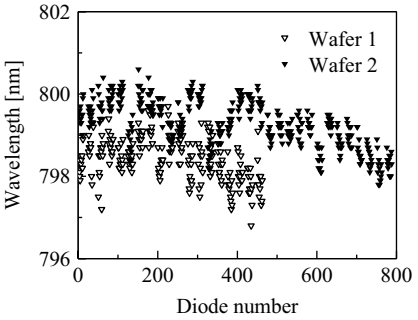

FIGURE 2.37. Peak wavelength distribution over one production lot

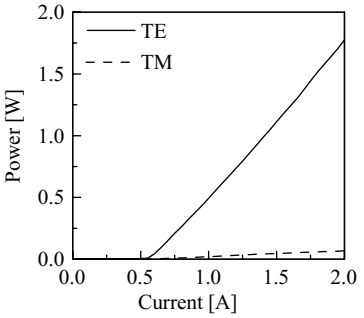

FIGURE 2.38. Light-current curve for TE and TM polarization

production lot. The wavelengths vary only by ± 1.5 nm. Therefore, the spectral emission of all bars fit into a window of only 4 nm. Based on this behavior, it is theoretically feasible to combine the power of upto ≈ 50 lasers with different wavelength in the 0.8–1.0 μm window by multiplexing and enhance the power in a laser beam for future applications. Practical designers have to consider the bandwidth of lasers and filters and therefore combinations of about six wavelengths are possible. Current systems rely on the few wavelength windows available today. Most often bars with 808-, 880-, 915-, 940-, and 980-nm are used.

2.4.2.3. Polarization

Polarization multiplexing (cf. Chapter 4.3.1) allows us to double the local power density in a laser beam further at an unchanged beam parameter product. The use of this technique requires a high degree of polarization in laser emission. Figure 2.38 shows the linear PI-characteristics for TE and TM polarization of an 808-nm AlInGaAs laser diode. It becomes evident that the optical power is mainly emitted in TE polarization, since the threshold for TM polarised laser emission is significantly higher and, as a consequence, the power emitted (at the operating point) in TE polarization exceeds TM polarized power by more than one order

of magnitude. The preferred polarization and the degree of polarization depend mainly on the strain in the device itself and especially in the QWs. For AlInGaAs QWs grown on a GaAs substrate, the QW material is compressively strained.

For QWs containing phosphorous, the strain is tensile and the band diagram is changed in a different way. As a result, the emission from aluminum-free QWs containing phosphorous is TM polarized. For practical applications, the degree of polarization and not the mode distribution represents the crucial figure.

2.4.2.4. Spatial Emission Pattern

To combine the emission from several diode lasers out of one bar into a single nearly circular spot, and/or, in a second step, to combine beams from different stacks, and to finally feed the emitted light into a glass fiber (for further details see Chapter 4.5), it is necessary to collimate the emitted light using optical elements such as lenses or lens-like structures. The design of efficient optical systems takes care of the far-field pattern. Current diode lasers exhibit asymmetrical far fields. Figure 2.39, shows the horizontal (a) and vertical (b) emission pattern of a laser. As the focusability of the light must not change during operation, it is important to have a narrow far-field during the whole operating time. The data were measured in cw-operation after a total operating time of 9,000 h for the device. In the horizontal direction (a), it exhibits a modulated far-field with a typical FWHM of about 10° due to multiple horizontal modes supported by the device. The pattern in the vertical direction, in contrast, has a FWHM of ≈35° at a near Gaussian shape. This Gaussian shape indicates that only the fundamental mode is emitted. The exact shape of the far-field pattern depends on the underlying layer structure, the contact design, the packaging and the operating conditions. For illustration, Fig. 2.40 depicts the far-field pattern for currents of 20 A (just above threshold) and 80 A (above the maximum specified operating current).

At low current densities, the FWHM is 4° and 34° in horizontal and vertical direction, respectively. At higher currents slow-axis FWHM rises to 5.9°, whereas the fast-axis FWHM remains stable as a consequence of the vertical single mode

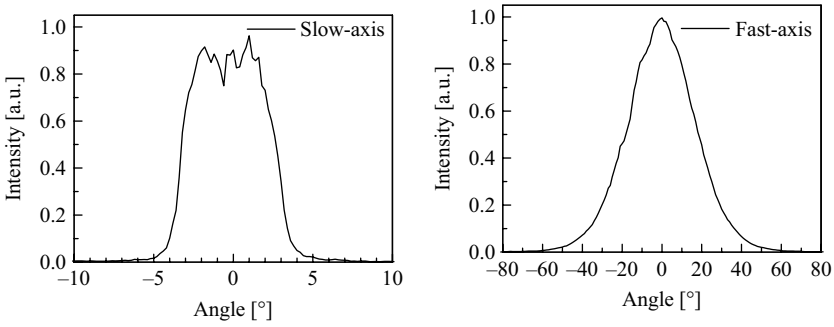

FIGURE 2.39. Far-field emission pattern for a 980-nm high-power diode laser bar after 9,000 h of continuous operation

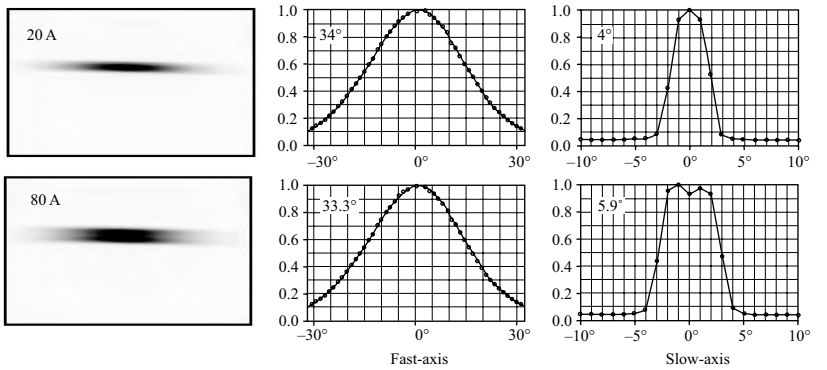

FIGURE 2.40. Far-field pattern at different operation currents. The last axis hardly changes between just above threshold (20 A) and at high current levels (80 A), while the slow-axis gradually widens: The FWHM increases from 4° to almost 6°

operation. The slow-axis, however, can emit higher-order modes whose mixture shows rather chaotic behavior caused by little changes of current, feedback from outside the laser back into the diode, and temperature distribution. Section 2.5 discusses developments which target at improved control of this spatial emission in the horizontal direction.

2.4.3. Lifetime and Reliability

The lifetime of semiconductor lasers depends on the operating conditions, in particular the applied current, the temperature within the active region, and the optical output power at the chip end facets. The temperature has a great impact on the aging behavior. As can be seen in section 2.1, the temperature increases the threshold current and reduces the slope efficiency simultaneously. Therefore it reduces the wall plug efficiency of the device and increases parasitic heat. Diffusion processes, the increased growth of defects, and their increased mobility at higher temperatures further promote the degradation of diodes. Figure 2.41 (left) compares the degradation of lasers bars of the same structure but operated at two different heat sink temperatures by displaying the output power versus time at a constant driving current. Obviously, the emitted power of the laser bars running at room temperature degrade only 0.5% during the first 500 h. In contrast, the bars operated at a heat sink temperature of 50°C degrade by about 5% of the original power after the same time.

The acceleration of degradation with increasing device temperature can be described by

$$AF_{th} \approx \exp\left[\frac{E_a}{k}\left(\frac{1}{T_1} - \frac{1}{T_2}\right)\right] \tag{2.32}$$

an exponential dependence of the acceleration factor (AF). When depicted in a semi-logarithmic plot, the lifetime versus temperature shows a linear relationship.

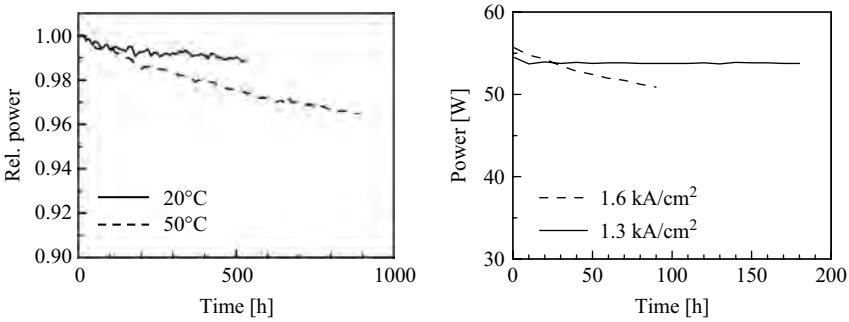

FIGURE 2.41. Output power over time: Left part: at 20°C and 50°C sub-mount temperature. Right part: for different current densities

The slope of the corresponding straight line is designated as the activation energy E_a. Typical values for high-power diode lasers in the InAlGaAs material system for an emission wavelength between 780 and 1,000 nm are between 0.3 and 0.5 eV.

In addition, the current density and the density of the optical power at the mirror facet have impact on the lifetime of the device. While the optical power density mainly enhances degradation in the mirror or in the region close to the mirror, the density of the applied current mainly affects the degradation of the semiconductor bulk material. In addition, the influence of current and optical power are interdependent, since the optical power is increased by an increasing current. Furthermore, a high optical power density can also interact with defects located inside the laser structure. To compute the total expected lifetime, one has to form the product of the different acceleration factors for temperature, current, and power. Nevertheless, the validity of this acceleration factors is limited only to a certain range of operation conditions without catastrophic degradation. Extreme current densities yield new degradation mechanisms that do not play a significant role under normal circumstances. Figure 2.41 (right part) depicts such degradation for laser structures operated at different current densities. While one structure quickly degrades to about 90% of the initial output power, the other structure remains almost stable during the first 200 h. The power density and the temperature of both structures were almost identical, but the current density differed by 30% . The different current density alone cannot explain the different degradation of the devices.

The lifetimes and output powers of diode lasers have been steadily increased over the last decades. Figure 2.42 (left part) shows the emitted output power per package or per laser bar over the last 40 years. The available cw power was increased from $P \approx 2.4\,W$ in 1984 to over $P \approx 20\,W$ in 1998 to 70–80 W in 2002. This steady increase was made possible by improvements in packaging technology and device efficiency. Figure 2.42 (right part) displays the emitted power at a constant driving current over lifetime. The data were taken from five laser bars with a fill factor

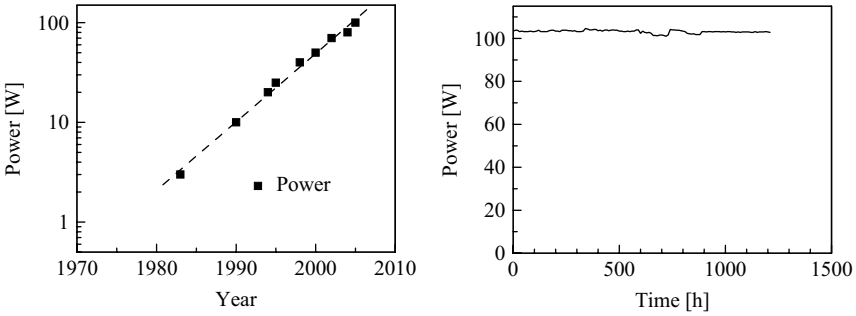

FIGURE 2.42. Development of output power per package during the last 40 years (left), and current test of 100 W/laser bar (right)

of 50% at a wavelength of 940 nm. At the beginning of the test the power level was at slightly above 100 W per bar. It can be seen that the output power changes little over the first 1,200 h with a degradation rate of less than 1% per kh. It becomes obvious, that today's power laser can be used upto 100 W and it has to be stated that the power is produced and emitted with an efficiency of more then 65%.

Recently, different operating conditions for power lasers became more important. Instead of a continuous-wave operation, a pulsed mode with a frequency of only a few Hertz and a duty cycle of upto 50% became more relevant for practical applications, e.g., welding or soldering in an industrial environment. This operating mode leads in addition to increased temperature, current, and power to increased thermo-mechanical stress cycles, enhancing the degradation. This stress is caused by the different thermal expansion coefficients of semiconductor and the commonly used copper heat sinks (see Chapter 3). The periodic heating or cooling of the device turns out to be equivalent to periodically changing the strain in the laser bar. It triggers other degradation mechanisms and leads to shorter lifetimes or even to spontaneous failures. To overcome this phenomenon, packaging as well as diode laser and operating conditions have to be designed to match the mutual needs. Today, laser bars that can survive more than 70 million cycles with a failure rate $<2\%$ can be designed.

2.5. High-Brightness Emitters and Arrays

Marc Kelemen

High-power high-brightness diode lasers are attracting more and more interest for applications previously dominated by expensive and inefficient solid-state lasers due to their better efficiency, compactness, and reliability. The significant fact about conventional high-brightness optical sources is that they exhibit about an

order-of-magnitude higher brightness than semiconductor lasers. The brightness is defined as

$$B = \frac{P}{A\Omega} \tag{2.33}$$

where P is the optical output power, A the emitting area, and Ω the solid angle into which the power is emitted. For a tapered diode laser this definition leads approximately to [2.44]

$$B = \frac{P}{\lambda_0^2 M_\perp^2 M_\parallel^2} \tag{2.34}$$

where λ_0 is the vacuum wavelength and M^2 the beam propagation parameter perpendicular ($M_\perp^2$) and in the plane ($M_\parallel^2$) of the epitaxial layer.

Today broad-area diode lasers are used to achieve high outputs. But standard broad-area waveguide designs are susceptible to modal instabilities, filamentation, and catastrophic optical mirror damage (COMD) failure [2.45]. This results in low beam qualities and values for the brightness limited to around $1 \times 10^7\ \mathrm{Wcm^{-2}sr^{-1}}$. On the other hand, high beam qualities are realized with ridge lasers emitting in a diffraction limited optical beam. The reliable output power of these lasers is mainly limited by the onset of facet degradation, which depends on the power density on the facet. Due to the small stripe width of a few microns, the output power is typically limited to about 700 mW, resulting in a brightness of less than $7 \times 10^7\ \mathrm{Wcm^{-2}sr^{-1}}$ [2.46].

A lot of different solutions have been proposed in the last few years to overcome these problems and to achieve high output power together with high beam quality. The main effort has been directed to develop broad-area structures that support only one lateral mode. Tapered devices [2.47, 2.48], distributed-feedback (DFB) lasers [2.49, 2.50], and monolithically integrated master-oscillator power amplifiers (MOPAs) [2.51] have been demonstrated, and all of them are able to produce output powers well above 1 W together with a high beam quality.

Among these, devices based on laterally tapered gain sections in combination with ridge-waveguide sections as depicted in Fig. 2.43 seem to be the most promising candidates when reproducible and low-cost fabrication is required. For the other concepts a costly epitaxial regrowth step or the fabrication of a holographically defined reflection grating is necessary, lowering the manufacturing yield. Tapered diode lasers produce diffraction limited output powers upto several watts in cw operation. The value of the brightness for a 1 W laser emitting a diffraction-limited beam at 1 μm wavelength is $10^8\ \mathrm{Wcm^{-2}sr^{-1}}$ according to Eq. (2.34). Hence tapered diode lasers provide a brightness upto a few times $10^8\ \mathrm{Wcm^{-2}sr^{-1}}$ in comparison to the few $10^7\ \mathrm{Wcm^{-2}sr^{-1}}$ of conventional semiconductor lasers.

This chapter is focused on the design and the performance of high-power diode lasers comprising ridge and tapered sections for near diffraction limited output power in the multiwatt regime optimized for the GaAs-based wavelength ranges between 880 and 1040 nm. It gives an overview of experimental work that has been

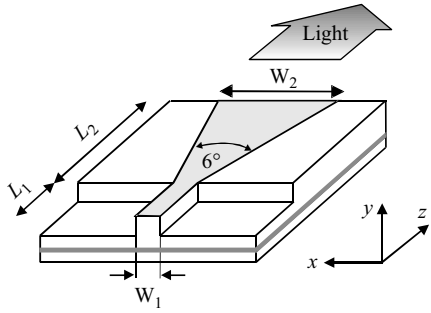

FIGURE 2.43. Schematic of a tapered diode laser with a ridge waveguide for mode filtering. The length L_1 of the ridge section is 500 μm. A taper angle of 6° together with a taper section length L_2 of 2 mm leads to an emitting aperture W_2 of about 200 μm

carried out in order to improve the beam quality as well as to enhance the output power of these devices. In the next section some theoretical background concerning the beam filamentation process and the far-field of devices with tapered gain regions is presented. The second section contains a description of the typical layer structure and fabrication process of the tapered diode lasers. The following sections contain an extensive review of experimental data, including output power, lifetime, beam quality, and astigmatism. The chapter concludes with a short description of tapered diode laser arrays comprising 19 tapered laser diodes.

2.5.1. Theoretical Background

2.5.1.1. Causes of Filamentation Processes

In broad-area devices, beam filamentation is the main physical effect that limits the device performance when high beam quality is required. With increasing power levels, spatial-hole burning occurs due to the interaction between the amplified optical field and the carrier density in the active region. Therefore, the complex optical index becomes inhomogeneous and leads to self-focusing of the optical wave. This results in filament formation, which severely deteriorates the beam quality [2.52].

The dependence of the complex optical index n on the carrier density n_c of the active layer is given by the following [2.53]:

$$n(n_c) = n_0 - \frac{1}{2k_0} g_m(n_c) \cdot \alpha_H + \frac{i}{2k_0}[g_m(n_c) - \alpha_i] \tag{2.35}$$

In this equation, $g_m(n_c) = \Gamma g(n_c)$ is the modal optical gain given by the product of the material gain $g(n_c)$ and the optical confinement factor Γ. The optical confinement factor is determined by the overlap between the vertical mode profile in the waveguide structure and the active layer. α_H is the linewidth enhancement factor, k_0 the vacuum wavenumber, n_0 the carrier independent part of the optical index, and α_{opt} are the total optical losses, respectively.

In order to achieve lateral coherence and to suppress filament formation in semiconductor lasers to reach high brightness, three principles are crucial:

- The differential optical index $\delta n(n_c)$ is proportional to the linewidth enhancement factor α_H. By finding ways to lower α_H, it is therefore possible to reduce the sensitivity against self-focusing and filamentation. For example, diode lasers based on quantum dot structures have been shown to possess an inherently low linewidth enhancement factor. Especially for tapered diode lasers, an increase of the ridge and taper section length further lowers the linewidth enhancement factor [2.54].
- Minimizing the optical losses α_{opt}. Using different lengths of the ridge and the taper sections of a tapered diode laser can change the optical losses. In addition the anti-reflection coating can be varied. In the case of a tapered diode laser the optical losses consist of the internal optical losses α_i, the resonator losses α_R and additionally a geometrical part (as additional resonator losses) due to the tapered resonator design which is well described in [2.53]:

$$\alpha_{opt} = \alpha_i + \alpha_R - \frac{1}{2(L_1 + L_2)} \ln\left(\frac{W_1^2 n_{eff}}{4\lambda_0 L_2}\right) \tag{2.36}$$

- As has been theoretically and experimentally analyzed in [2.55, 2.56], the differential optical index $\delta n(n_c)$ is proportional to the square of the confinement factor. So, a reduced confinement factor also reduces the variation of the optical index due to spatial-hole burning. This can be realized through epitaxial design, as described in the next section.

2.5.1.2. Astigmatism and Corrected Far Field

In order to determine whether the beam quality is diffraction limited, the measurement of interest is not the angular width of the output beam (far field) as normally used for broad-area diode lasers, but rather a measurement that is more sensitive to beam quality, a measurement of the beam at a waist called "corrected far-field" [2.44, 2.47].

At the output facet the curved wavefronts of tapered diode lasers diffract according to Snell's law and the beam will propagate with a width that is approximately n_{eff} times the internal full taper angle. With a taper angle of 6° this product yields a beam about 20° wide. The beam is astigmatic, since in the direction perpendicular to the quantum well it diverges from the output facet, but in the plane of the quantum well it diverges from a virtual source that is approximately L_2/n_{eff} behind the output facet inside the device. Because n_{eff} is dependent on the carrier density and the temperature, distortions of the carrier distribution or different thermal management concepts have a remarkable influence on n_{eff} and on the position of the virtual source [2.57].

For the measurements, a spherical lens is used to collimate the beam in the fast-axis direction (vertically) as shown in Fig. 2.44. Because of the astigmatism, the beam is focused in the lateral plane resulting in a waist w_{ff}, called corrected

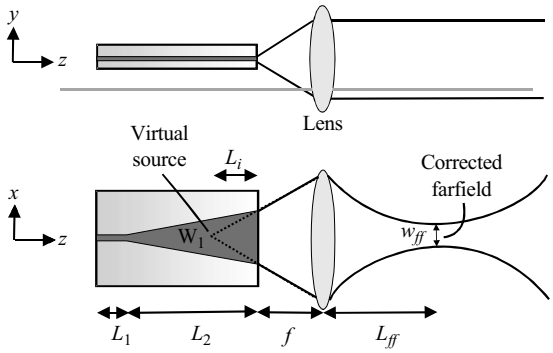

FIGURE 2.44. Schematic of an astigmatism measurement. A lens is used to collimate the beam in the fast-axis direction (vertically). Because of the astigmatism, the beam is focused in the lateral plane resulting in a waist, called corrected far field

far field. The distance L_{ff} between lens and corrected far field provides a direct measure of the astigmatism using the lens equation and the known focal length f of the measurement lens. Similarly, the width w_{ff} of the waist is a measure of the width of the virtual source.

It can also be shown that a lateral scan of the power distribution at this waist is exactly the same as the power distribution that would be found at a focal length beyond the measurement lens if an ideal thin cylindrical lens had been placed at the output facet to collimate the beam in the lateral plane; (removal of the quadratic phase curvature due to the divergence of the beam). Hence, the relative power density measured at the waist as a function of the lateral distance x is a direct measure of the far-field pattern with the quadratic phase curvature removed, if one interprets ϕ as:

$$\phi = \arctan(x/f) \tag{2.37}$$

This ideal beam is convenient to be used as a benchmark for the beam quality of real beams. For an ideal top hat distribution the full width half-maximum angle ϕ_{FWHM} for the far-field distribution of the power density is [2.44]:

$$\phi_{FWHM} \approx 0.84\lambda_0/\mathrm{W}_2 \tag{2.38}$$

If the near-field profile is not top hat but rather Gaussian (if gain saturation plays no role), the far-field distribution as Fourier transformation of the Gaussian near-field distribution has a factor of 1.5 instead of 0.84 for the full width half maximum angle in Eq. (2.37).

2.5.2. Fabrication of Tapered Devices

The fabrication of high brightness lasers with high conversion efficiency requires an epitaxial layer sequence with low internal losses ($<2\mathrm{cm}^{-1}$), low confinement

factor (<1.5%) and high internal conversion efficiency (>0.9). The reduction of the internal losses and of the confinement factor can be achieved by broadening the waveguide layers [2.58]. This reduces the overlap of the optical mode with the highly doped cladding layers. Generally the laser structures were grown by molecular beam epitaxy (MBE). As an example the typical fabrication process of a tapered diode laser emitting at 940 nm is described in detail in the following.

1. The active region consists of a single InGaAs-quantum well embedded in an 880 nm thick AlGaAs core region with 20% Al content. For 940 nm the quantum well is 7 nm thick with a nominal Indium content of 12% . The optical waveguide is formed by 1 μm thick AlGaAs claddings with 40% Al. Si and Be are used for n- and p-type doping, respectively. The doping concentrations start at a level of $5 \times 10^{17}\,\mathrm{cm}^{-3}$ near the core and increase to a level of $2 \times 10^{18}\,\mathrm{cm}^{-3}$ in the outer cladding regions. The GaAs cap layer is highly p-doped ($6 \times 10^{19}\,\mathrm{cm}^{-3}$) in order to reduce the contact resistance. The layer design exhibits an overlap of the fundamental optical mode with the quantum well of 1.3% at 940 nm. It has been shown previously that this low modal gain epitaxial layer structure suppresses beam filamentation in tapered laser oscillators and tapered laser amplifiers [2.56]. As a further advantage of this layer sequence, 95% of the optical power is concentrated in the undoped core layers and the overlap of the fundamental mode with the doped cladding layers is only 5% . As a result, low internal losses of $1.5\,\mathrm{cm}^{-1}$ are obtained, measured on Fabry-Perot laser diodes of different lengths. The high material quality of the MBE-grown laser structures yields a high internal efficiency of more than 90%. The use of high-band-gap ($E_g = 1.68\,\mathrm{eV}$) AlGaAs core layers with 20% of Al content leads to a strong carrier confinement. This results in laser diodes with relatively temperature insensitive characteristics. Experimentally, a characteristic temperature of $T_0 = 160\,\mathrm{K}$ is observed for broad area diode lasers in the temperature range between 15°C and 80°C.
2. From this material diode lasers comprising a ridge section as well as a tapered section have been fabricated in a standard process [2.53]. Figure 2.43 shows a schematic of the device. A typical structure for tapered diode lasers consists of a taper angle of 6° together with a taper section length of 2 mm. This leads to an emitting aperture of about 210 μm width. The length of the ridge section is $L_1 = 500\,\mu\mathrm{m}$, resulting in a total device length of 2.5 mm.
3. After thinning and cleaving a highly reflective double-stack of Si and SiO_2 (95% reflectivity) is deposited on the back facet by reactive magnetron sputtering. Two different anti-reflection coatings are used for the front-facet: (i) a single layer of SiN (<1% reflectivity) and (ii) a single layer of SiON (<0.01% reflectivity). In principle this device can function as either an amplifier [2.47] or a laser depending on the rear facet coating.
4. Finally the devices are mounted p-side down on copper mounts (C-mounts) with indium solder. Uniform pumping of the laser medium is achieved by current injection via bond wires.

The epitaxial layer sequences and fabrication processes of the GaAs based tapered diode lasers emitting between 880 nm and 1040 nm are similar and reported in [2.56].

2.5.3. Characterization and Results of Single Emitters

2.5.3.1. Electro-Optical Characterization

Figure 2.45 shows a typical P-I-characteristic together with the wall plug efficiency of a tapered diode laser emitting at 940 nm at a heat sink temperature of 20°C [2.59]. The length of the taper section is 2 mm and the length of the ridge section is 0.5 mm. The anti-reflection coating is provided by SiON resulting in a reflectivity of less than 0.01% . The device shows a comparatively low threshold current of 0.78 A corresponding to a threshold current density of 400 A/cm^2. The maximum slope efficiency of 0.88 W/A together with the low series resistance of 30 mΩ results in a high conversion efficiency. At 4 W of output power a maximum wall plug efficiency of 45% is achieved.

The emission spectra of the devices have a spectral width (FWHM) of 3 nm at 4 A. From the shift of the peak emission wavelength with driving current a total thermal resistance of 7 K/W can be deduced for the complete experimental setup including the thermoelectric cooling of the C-mount heat sink.

For tapered diode lasers emitting at other wavelengths similar results have been reached [2.59–2.61]. Figure 2.46 summarizes typical P-I-characteristics for

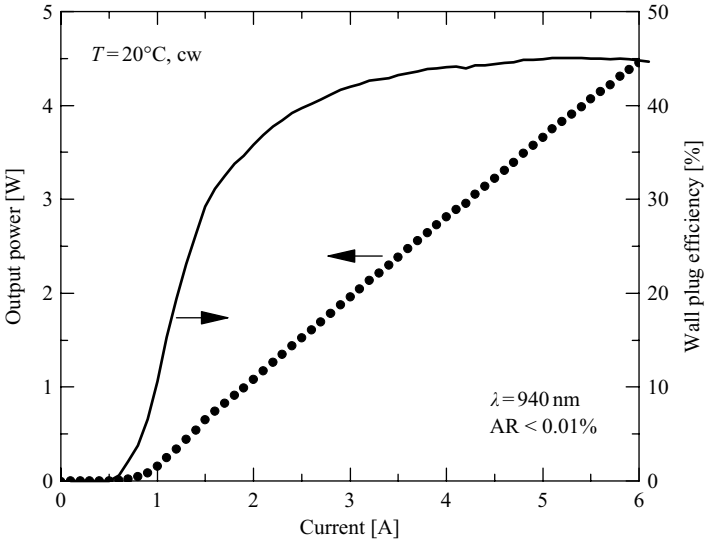

Figure 2.45. Typical current-power characteristic and wall plug efficiency of a tapered diode laser emitting at 940 nm. The measurements have been done at a heat sink temperature of 20°C and in continuous-wave mode

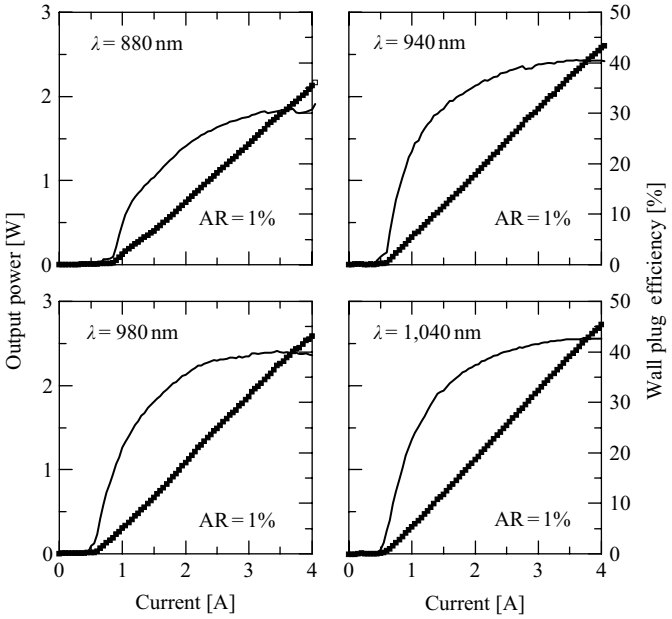

FIGURE 2.46. Typical current-power characteristics and wall plug efficiencies of tapered diode lasers emitting at different wavelengths. The measurements have been done at a heat sink temperature of 20°C and in continuous-wave mode

TABLE 2.5. Electro-optical characteristics of tapered lasers with different emission wavelengths

λ (nm)	880	940	940	980	1040
AR(%)	1	1	0.01	1	1
I_{th} (A)	0.85	0.60	0.78	0.64	0.62
J_{th} (A/cm^2)	440	310	400	330	320
s.e. (W/A)	0.66	0.77	0.88	0.80	0.81
P_{4A} (W)	2.1	2.6	2.8	2.6	2.7
η_{4A}(%)	30	40	44	39	43

tapered diode lasers emitting between 880 nm and 1040 nm. In contrast to Fig. 2.45 the anti-reflection coating in this figure is provided by SiN resulting in a reflectivity of 1% in order to reduce the threshold current. For all wavelengths output powers of more than 2 W have been reached at a current of 4 A. The threshold currents are between 0.6 A for 1040 nm and 0.85 A for 880 nm. Slope efficiencies (*s.e.*) between 0.81 W/A and 0.66 W/A have been measured together with corresponding wall-plug efficiencies between 30% for 880 nm and 43% for 1040 nm. Table 2.5 summarizes the main results of the electro-optical characterization for the tapered diode lasers emitting between 880 nm and 1040 nm.

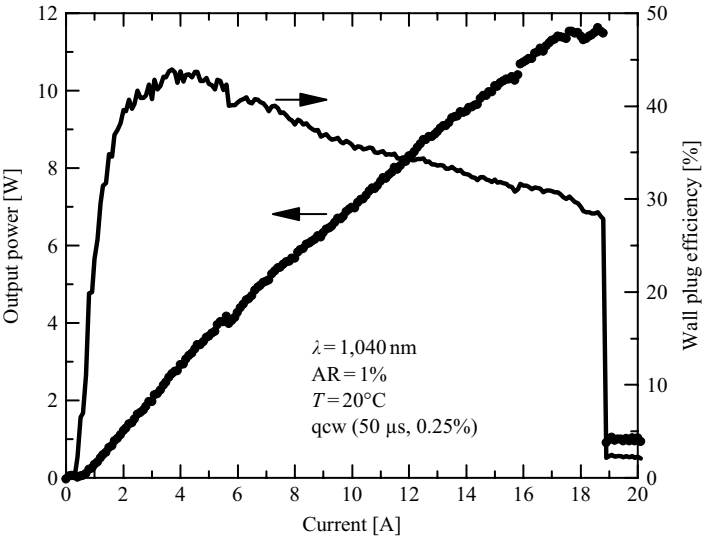

FIGURE 2.47. Typical current-power characteristic and wall plug efficiency of a tapered diode laser emitting at 1040 nm. The measurements have been done at a heat sink temperature of 20°C and in quasi-continuous-wave mode (50-µs pulse time, 0.25% duty cycle)

In order to investigate the limitation on the output power and the stability of the output facet, the driving current can be ramped up in quasi-continuous-wave (qcw) mode to the point of sudden failure. In Fig. 2.47 the qcw mode was realized by a pulse time of 50 µs and a duty cycle of 0.25%. A record of 11.6 W output power for single tapered diode lasers was achieved at a driving current of 18.5 A. At 18.8 A catastrophic optical mirror damage occurred at the front facet. The power density at the emitting facet is estimated to be about 6 MW/cm^2, which is comparable to broad-area diode-lasers [2.61].

As an example the long-term reliability of the tapered diode lasers emitting at 1040 nm has been tested by aging a batch of six devices at a heat sink temperature of 50°C [2.61]. Under constant current condition at 4 A (Fig. 2.48) the output power is 2 W. All devices show only gradual degradation within the first 1,100 h without sudden failure. Defining a 20% decrease of the output power as a criterion for the lifetime, an extrapolated lifetime of more than 10,000 h can be deduced for a heat sink temperature of 50°C. Under a cautious assumption of 0.2 eV for the activation energy, a lifetime of more than 20,000 h at room temperature can be deduced from these data. The beam quality parameter M^2 remains unchanged after the accelerated aging. In addition lifetimes of more than 10,000 h have been demonstrated for tapered diode lasers emitting at 940 nm and 980 nm.

2.5.3.2. Beam Quality and Brightness

The useful output power of tapered devices is limited by the deterioration of the beam quality with increasing power. For this it is instructive to look at the

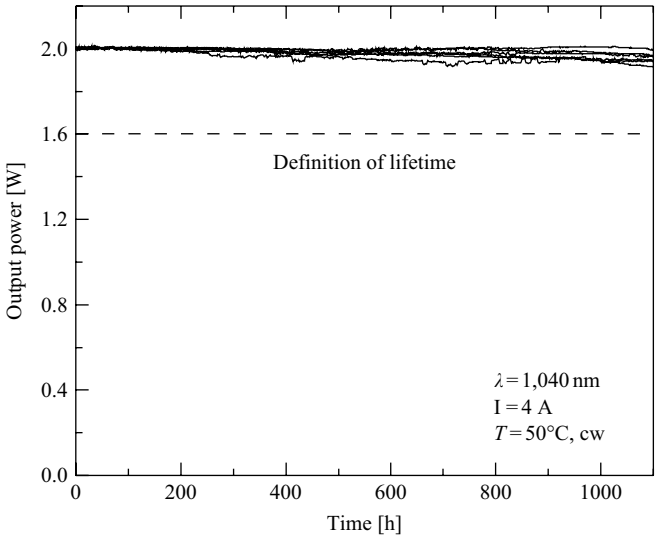

FIGURE 2.48. Reliability test of a batch of six tapered diode lasers at an output power of 2 W and a heat sink temperature of 50°C. A lifetime of more than 20,000 h can be deduced from these data at 20°C

illumination patterns at the output facet, often called near-field patterns. The structure observed in the near-field is mostly closely related to the effects inside the tapered gain region that degrade the beam quality. These patterns simply show the relative power density at the facet and do not provide a measure of the phase, which to first order one expects to vary quadratically across the facet [2.44]. Figure 2.49 shows the dependence of the beam profile at the facet (near-field) on the output power for a tapered diode laser emitting at 1040 nm. Upto 3 W the near field profiles can be described with Gaussian curves demonstrating the diffraction limited behavior. For higher output powers slight filamentation effects occur.

In order to investigate the beam quality of tapered laser oscillators, the beam quality parameter M^2 was measured after ISO 11146 with a commercial beam analyzing system (DataRay Beam Scope).

The dependence of the beam quality parameter M^2 on the output power is shown in Fig. 2.50 for tapered diode lasers emitting at different wavelengths [2.54, 2.60, 2.62]. All diodes consist of a taper section length of 2,000 μm and a ridge section length of 500 μm. A beam quality parameter as low as $M^2 = 2$ or less is achieved at an output power of 2 W for all wavelengths except 880 nm. At 1040 nm the beam quality remains nearly diffraction limited upto output powers of 3 W due to the lowest confinement factor ($\Gamma = 1.1\%$) of all tapered diode lasers investigated.

In good accordance to the predictions given in section 2.5.1 the experimental results further show that the length of the ridge and the taper sections have a strong impact on the beam quality at high output powers. In Fig. 2.51 tapered diode lasers

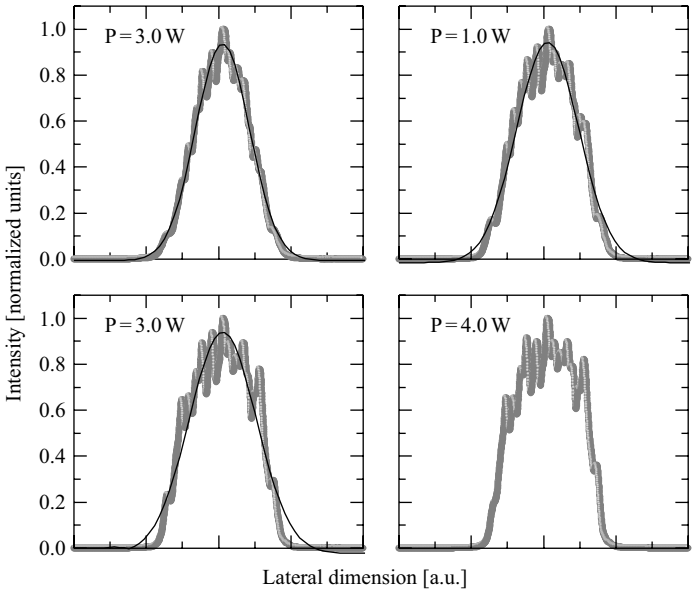

FIGURE 2.49. Dependence of the near-field profiles of tapered diode lasers emitting at 1040 nm on the output power at a heat sink temperature of 20°C (cw). The Gaussian-like fit curves demonstrate the nearly diffraction limited behavior of the tapered diode lasers up to 3 W

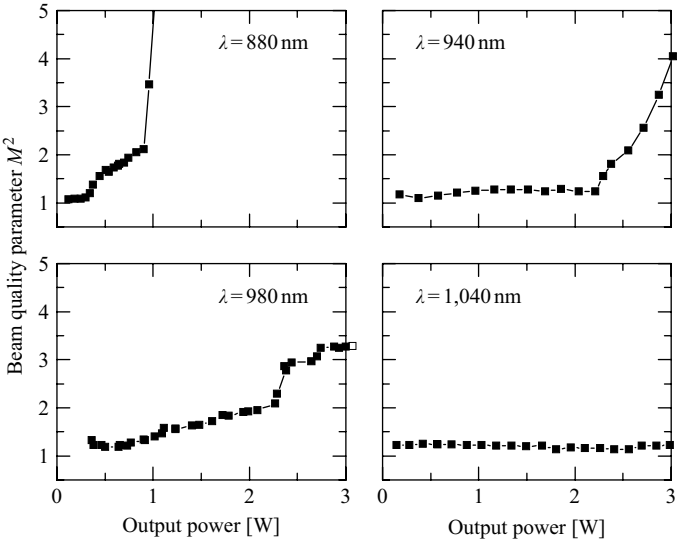

FIGURE 2.50. Typical M^2 characteristics of tapered diode lasers emitting at different wavelengths in dependence on the output power. The measurements have been done at a heat sink temperature of 20°C and in continuous-wave mode

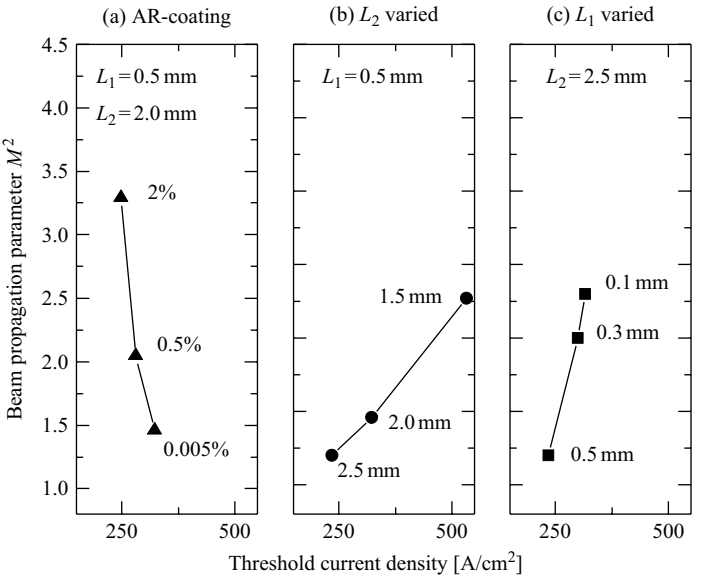

FIGURE 2.51. Typical M^2 characteristics of tapered diode lasers emitting at 940 nm in dependence on the (a) anti-reflection coating (b) taper section length L_2, and (c) ridge section length L_1. The measurements have been done at a heat sink temperature of 20°C and in continuous-wave mode at a power level of 1 W

emitting at 940 nm are shown for different lengths of the ridge and the taper section as an example. For a ridge length of 100 μm the beam quality starts to decrease rapidly at a power level of $P = 1$ W. In contrast to this result, the beam quality of the devices with ridge lengths of $L_1 = 500$ μm remain in the range of $M^2 < 1.5$ upto more than 2 W of output power. In addition, a longer taper section length also enhances the beam quality. Whereas the beam quality of devices having a taper length of 2,000 μm remains nearly diffraction limited upto about 2.2 W with an M^2-value of 1.3, a taper section length of 1,500 μm causes M^2 to increase rapidly above a lower power level of about 0.4 W. It has been shown that the increase of the length of one or both sections lowers the linewidth enhancement factor and leads to a lower tendency of filamentation and hence to a better beam quality [2.54].

With increasing output facet reflectivity, an increasing percentage of the optical field is reflected into the resonator enhancing the formation of dynamically varying longitudinal and transverse structures in the intensity distribution [2.47]. Therefore it is reasonable to reduce the facet reflectivities as far as possible to avoid such a phenomenon. In Fig. 2.51 anti-reflection coatings down to 0.005% have been used to further improve the beam quality. But it may be advantageous to accept higher facet reflectivities to reduce backward reflections from optical components like lenses and fibers. So for practical reasons an anti-reflection coating of 1% is frequently used today.

2.5.3.3. Corrected Far-Field and Astigmatism

Far-field profiles of the devices were measured after correcting for the quadratic phase front divergence by using a cylindrical lens (corrected far field) according to section 2.5.1. An example for the evolution of the lateral far-field profiles of tapered diode lasers with increasing output power can be seen in Fig. 2.52. A power independent far field angle of 0.24° (FWHM) is obtained for the full range of cw output powers [2.59]. This value is equal to 1.06 times the value predicted by Eq. (2.5). The fraction of power at 3 W contained inside the central lobe is 93% (2.8 W). To estimate the brightness (P/λ^2) of this source, one can use the power in the central lobe divided by ($1.06 \cdot \lambda^2$), where the factor 1.06 has been added to the denominator to account for the increase in the far-field angle above the diffraction limit. The result is a brightness value of $3.0 \cdot 10^8\ \mathrm{Wcm^{-2}sr^{-1}}$.

The measured M^2-parameters in Fig. 2.52 range between 1.1 at 1 W and 4.1 at 3 W of output power. The growth of side lobes at higher output powers is responsible for the increase of the beam quality parameter M^2. Conventionally beam diameters have been measured at the $1/e^2$ intensity point; i.e., at 13.5% of the maximum intensity. ISO 11146 requires the use of a "Second Moment" definition of beam diameter. For this reason the side lobes also increase the calculated beam quality factor M^2.

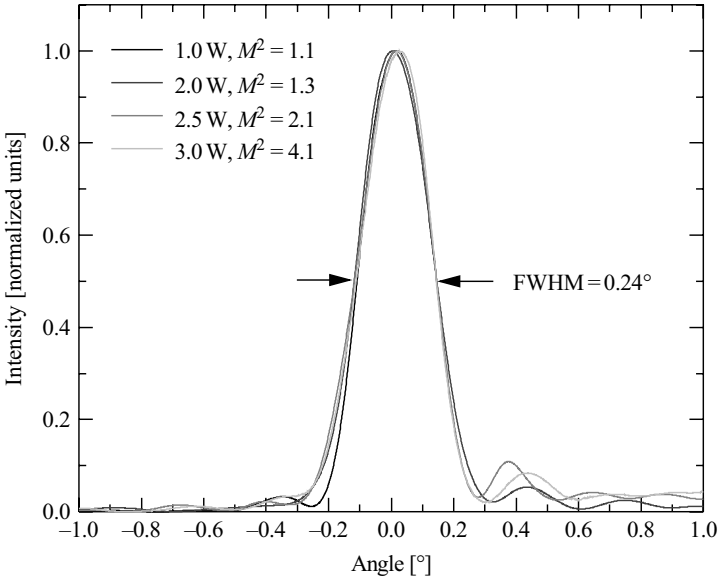

FIGURE 2.52. Dependence of the lateral far-field profiles of tapered high-power diode lasers on the output power after removal of the quadratic phase curvature by a cylindrical lens at a heat sink temperature of 20°C (cw). Additionally the measured values of M^2 are given corresponding to the output power

For the diodes emitting at 980 nm similar values for the corrected far field have been obtained [2.60]. For 1040 nm the far field distribution is more Gaussian like. In this case the measured values of 0.43° upto 4 W must be compared to the theoretical value of 0.40° for a Gaussian near field distribution. This value is equal to 1.03 at an output power of 4 W and results in a brightness of $3.6 \cdot 10^8$ $\mathrm{Wcm^{-2}sr^{-1}}$ [2.61].

In [2.62] the astigmatism curves (distance between virtual source and facet) in dependence on the current have been investigated for different design parameters. It has been shown experimentally that in the low current regime ($I < 3I_{th}$) the ridge and the taper section length have a significant influence on the position of the virtual source, visible in a change of the astigmatism. There is a weaker influence of the design on the astigmatism in the higher current regime ($I > 3I_{th}$).

The astigmatism of tapered diode lasers is mainly temperature driven, as shown in Fig. 2.53. A lower thermal resistance, leading to a better heat flow, results in a fast cross over into a flat curve. In contrast to this, higher values of the thermal resistance lead to a gradual change over to a flat behavior. As a result, the astigmatism remains nearly constant in the higher current regime respectively higher output regime. The same effect takes place by making the tapered section length longer. Here for longer tapered section lengths the power losses per area decrease, there is a better heat flow, and the astigmatism reaches saturation faster [2.62].

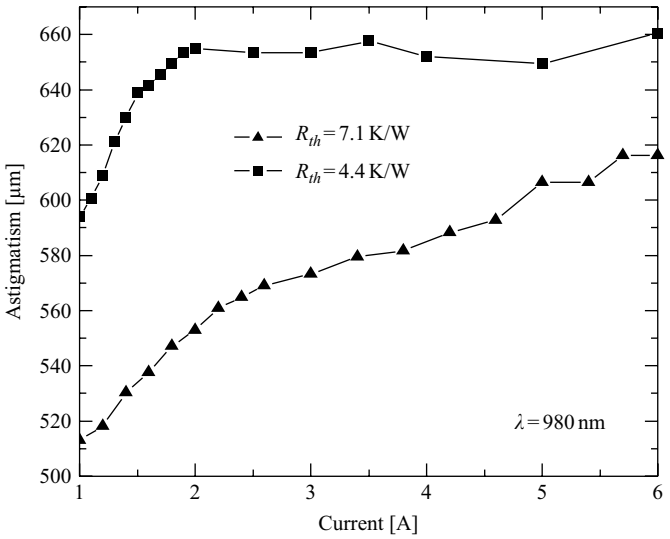

FIGURE 2.53. Astigmatism of tapered diode lasers emitting at 980 nm in dependence on the current for different thermal resistances. All measurements have been done at a heat sink temperature of 20°C in cw mode. The thermal resistance has been changed by using different heat sinks

2.5.4. Characterization and Results of High-Brightness Arrays

Depending on heat sink and facet preparation the available and reliable output power of a single tapered diode laser is restricted to a few Watts only. Therefore, it is straightforward to fabricate monolithically integrated diode laser arrays in order to achieve higher output powers and higher optical power densities. A diode laser bar with tapered lasers instead of broad area devices comprises 19 single emitters with 210 μm wide apertures and a pitch of 500 μm from laser to laser.

Figure 2.54 shows the P-I-characteristic of a tapered diode laser array together with its wall-plug efficiency. The device has a slope efficiency of 0.74 W/A, a threshold current of 10.5 A and a threshold current density of 380 A/cm^2. The array delivers nearly 30 W of optical output power under cw-operation and a driving current of 50 A which is limited by the current source. The output power is distributed fairly uniformly among the 19 emitters with an average of 1.54 W in very good agreement with the results of the single emitters shown in Fig. 2.45. No rollover occurs and the wall-plug efficiency does not reach its maximum in the observed current range, 38% is achieved at the highest output power. All measurements are performed at a heat sink temperature of 25°C.

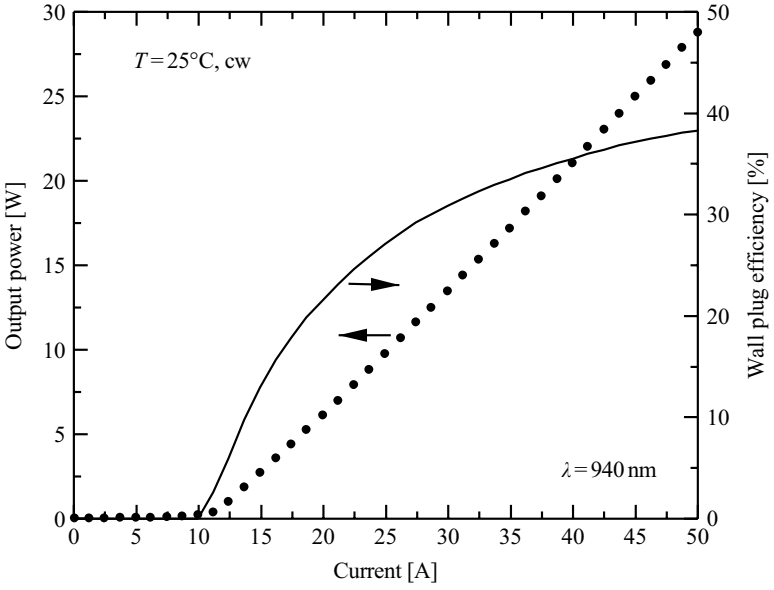

FIGURE 2.54. P-I-characteristic and wall plug efficiency of a tapered laser array emitting at 940 nm comprising 19 individual emitters. The measurements have been done at a heat sink temperature of 25°C and in continuous-wave mode

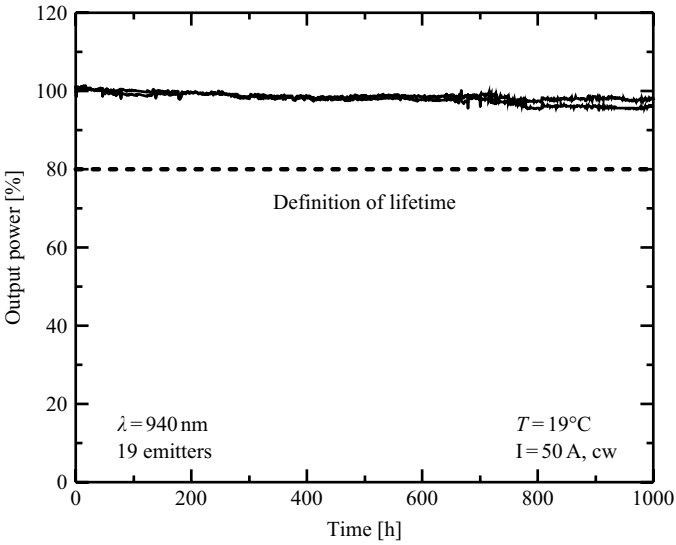

FIGURE 2.55. Reliability test of tapered laser arrays emitting at 940 nm at a current of 50 A and a heat sink temperature of 19°C in continuous-wave mode

The long-term reliability of the tapered laser array has been tested by aging two devices emitting at 940 nm at a heat sink temperature of 50°C (Fig. 2.55). Both devices show only gradual degradation within the first 1,000 h without sudden failure. Defining a 20% decrease of the output power as a criterion for the lifetime, an extrapolated lifetime of more than 5,000 h can be deduced for a heat sink temperature of 50°C.

List of Symbols

B	brightness
f	focal length of lens
g	material gain
g_m	modal optical gain
I_{th}	threshold current
J_{th}	threshold current density
k_0	vacuum wavenumber
L_1	length of ridge section
L_2	length of taper section
M^2	beam propagation parameter
n	complex optical index
n_c	carrier density
n_0	carrier-independent part of the optical index

n_{eff}	effective index of refraction
P	output power
$s.e.$	slope efficiency
W_1	width of the ridge waveguide
W_2	width of output facet
a	astigmatism
α_i	internal losses
α_R	resonator losses
α_{opt}	total optical losses
Γ	confinement factor
η	wall plug efficiency
η_i	internal efficiency
λ_0	vacuum wavelength
ϕ_{FWHM}	full-width half-maximum (FWHM) angle

References

[2.1] Koechner W (1966) Solid State Laser Engineering. Springer-Verlag, Berlin, Heidelberg, p. 82ff.

[2.2] Diehl R (ed.) (2000) High-Power Diode Lasers. Springer-Verlag, Berlin, Heidelberg.

[2.3] Carlsson NW (ed.) (1994) Monolithic Diode-Laser Arrays. Springer-Verlag, Berlin, Heidelberg.

[2.4] Suhura T (2004) Semiconductor Lasers Fundamentals. Marcel Dekker, Inc., New York, Basel.

[2.5] Tansu N, Mawst LJ (2002) Temperature sensitivity of 1300-nm InGaAsN quantum-well lasers. IEEE Photonic Technology Letters 14, 1052–1054.

[2.6] Haug A (1987) Relations between the T_0 values of bulk and quantum-well GaAs. Journal of Applied Physics B44, 151–153.

[2.7] Garbuzov D, Shiau GJ, Bulovic V, Boroditsky M, Chao CP, Forrest SR (1995) Photoluminescence study of excess carrier spillover in 1.3 μm wavelength strained multi-quantum-well InGaAsP/InP laser structures. Applied Physics Letters 66, 1307–1309.

[2.8] Lu H, Blaauw C, Makino T (1995) High-temperature single-mode operation of 1.3 μm strained MQW gain-coupled DFB lasers. IEEE Photonic Technology Letters 7, 611–613.

[2.9] Evans JD, Simmons JG, Makino T (1997) On the temperature sensitivity of strained multiple quantum well, long wavelength semiconductor lasers: Root cause analysis and the effects of varying device structures. Proceedings of the SPIE 3001, 218–234.

[2.10] Ishikawa M, Shiozawa H, Itaya K, Hatakoshi G, Uematsu Y (1991) Temperature dependence of threshold current for InGaAlP visible laser diodes. IEEE Journal of Quantum Electronics 27, 23–29.

[2.11] Manasevit HM (1969) The use of metal-organics in the preparation of semiconductor materials I. Epitaxial gallium-V compounds. Applied Physics Letters 116, 1725.

[2.12] Manasevit HM (1972) The use of metal-organics in the preparation of semiconductor materials: Growth on insulation substrates. Journal of Crystal Growth 13–14, 306.

[2.13] Miederer W, Ziegler G, Dotzer R (1962) German Patent 1,176,102.

[2.14] Shaw DW (1972) Kinetic aspects in the vapor phase epitaxy of III–V-compounds. Journal of Crystal Growth 31, 130.
[2.15] Reep DH, Ghandi SK (1983) Deposition of GaAs epitaxial layers by organometallic CVD. Temperature and orientation dependence. Journal of Electrochemical Society. 130, 675.
[2.16] Leys MR, Veenvliet H (1981) A study of the growth mechanism of epitaxial GaAs as grown by the technique of metalorganic vapor phase epitaxy. Journal of Crystal Growth 55, 145.
[2.17] Stringfellow G (1999) Organometallic vapor-phase epitaxy: Theory and Practice, 2nd Edition. Academic Press, San Diego.
[2.18] Richter W, Zettler JT (1996) Real-time analysis of III–V-semiconductor epitaxial growth. Applied Surface Science 100/101, 465.
[2.19] http://www.aixtron.com/.
[2.20] http://www.veeco.com/.
[2.21] Grovenor CRM (1992) Microelectronic Materials. Institute of Physics publishing, Bristol and Philadelphia, ISBN 0-85274-270-3.
[2.22] Thompson LF, Willson CG, Bowden MJ (1994) Introduction to Microlithography, 2nd Edition. American Chemical Society.
[2.23] Beneking H (1991) Halbleiter-Technologie, B.G. Teubner, Stuttgart.
[2.24] Adachi S, Oe K (1983) Journal of Electrochemical Society 130 and 12, 2427.
[2.25] Mattox DM (1998) Handbook of Physical Vapor Deposition (PVD) Processing. Noyes Publications.
[2.26] Sze SM (1981) Physics of Semiconductor Devices. John Wiley & Sons.
[2.27] Gasser M, Latta EE (1992) Method for mirror passivation of semiconductor laser diodes. US Patent No. 5144634.
[2.28] Tu L, Schubert E, Hong M, Zydzik G (1996) In-vacuum cleaving and coating of semiconductor laser facets using thin silicon and a dielectric. Journal Applied Physics 80(11), 6448.
[2.29] Collot P, Delalande S, Olivier J (1999) Sulphur passivation of dry-etched AlGaAs laser facets. Electronics Letters 35(6), 506.
[2.30] Ueda O (1996) Reliability and Degradation of III–V optical devices. Artech House.
[2.31] Xia R, Larkins EC, Harrison I, Dods SRA, Andrianov AV, Morgan J, Landesman JP (2002) Mounting induced strain threshold for the degradation of high power AlGaAs laser bars. Photonics Technology Letters 14, 893.
[2.32] Tomm JW, Gerhardt A, Elsaesser T, Lorenzen D, Hennig P (2002) Simultaneous quantification of strain and defects in high power diode laser devices. Applied Physics Letters 81, 3269.
[2.33] Tomm, JW, Gerhardt A, Müller R, Malyarchuk V, Sainte-Marie Y, Galtier P, Nagle J, Landesman JP (2003) Spatially-resolved spectroscopic strain measurements on high-power laser diode bars. Journal of Applied Physics 93, 1848.
[2.34] Gerhardt A, Weik F, Quoc Tran T, Tomm JW, Elsaesser T, Biesenbach J, Müntz H, Seibold G, Biermann ML (2004) Device deformation during low frequency pulsed operation of high power diode bars, Applied Physics Letters 84, 3525.
[2.35] Todoroki S, Sawai M, Aiki K (1985) Temperature distribution along the striped active region in hig-power GaAlAs visible lasers. Journal of Applied Physics 58, 1124.
[2.36] Brugger H, Epperlein PW (1990) Mapping of local temperature distributions on mirrors of GaAs/AlGaAs laser diodes. Applied Physics Letters 56, 1049.

[2.37] Tang WC, Rosen HH, Vettinger P, Webb DJ (1991) Raman microprobe study of the time development of AlGaAs single quantum well laser facet temperature on route to catastrophic breakdown. Applied Physics Letters 58, 557.
[2.38] Kranz MC, Rosen HJ, Lenth W (1990) Localized temperature dynamics of GaAlAs laser facets investigated by Raman microprobe measurements. El. Letters 26, 990.
[2.39] Tomm JW, Thamm E, Bärwolff A, Elsaesser T, Luft J, Baeumler M, Mueller S, Jantz W, Rechenberg I, Erbert G (2000) Facet degradation of high power diode laser arrays. Applied Physics A 70, 377.
[2.40] Puchert R, Tomm JW, Jaeger A, Bärwolff A, Luft J, Späth W (1998) Emitter failure and thermal facet load in high-power laser diode arrays. Applied Physics A 66, 483.
[2.41] Rinner F, Rogg J, Konstanzer H, Mikulla M, Weimann G, Tomm JW, Thamm E, Poprawe R (2003) Facet temperature reduction a current blocking layer at the front facets of high power InGaAs/AlGaAs lasers. Journal of Applied Physics 93, 1354.
[2.42] Herrmann FU, Beeck S, Abstreiter G, Hanke C, Hoyler C, Korte L (1991) Reduction of mirror temperature in GaAs/AlGaAs quantum well laser diodes with segmented contacts. Applied Physics Letters 58, 1007.
[2.43] Garbusov DZ, Abeles J, Morris NA, Gardner PD, Triano AR, Harvey MG, Gilbert DB, Conolly JC (1996) High power separate confinement heterostructure AlGaAs/GaAs laser diodes with broadened waveguide, SPIE Proceedings 2682, 20.
[2.44] Walpole JN (1996) Semiconductor amplifiers and lasers with tapered gain regions. Optical and Quantum Electronics 28, 623.
[2.45] Moser A, Latta EE (1992) Arrhenius parameters for the rate process leading to catastrophic damage of AlGaAs-GaAs laser facets. Journal of Applied Physics, 71, 4848–4853.
[2.46] Pawlik S, Traut S, Thies A, Sverdlov B, Schmidt B (2002) Ultra-high power RWG laser diodes with lateral absorber region. 18th IEEE International Semiconductors Laser Conference, Garmisch, Germany, 163.
[2.47] Kintzer ES, Walpole JN, Chinn SR, Wang CA, Missaggia LJ (1993) High power strained-layer amplifiers and lasers with tapered gain regions. IEEE Photon Technological Letters 5, 605.
[2.48] O'Brien S, Schönfelder A, Lang RJ (1997) 5W CW diffraction-limited InGaAs broad-area flared amplifier at 970 nm. IEEE Photon Technolgical Letters 9, 1217.
[2.49] de Mars SD, Dzurko KM, Lang RJ, Welch DF, Scifres DR, Hardy A (1996) Angles grating distributed-feedback laser with 1 W single-mode, diffraction-limited output at 980 nm. Technical Digest CLEO 96, 77.
[2.50] Paschke K, Bogatov A, Bugge F, Drakin AE, Fricke J, Guther R, Stratonikov AA, Wenzel H, Erbert G, Tränkle G (2003) Properties of ion-implanted hig-power angled-grating distributed-feedback lasers, IEEE Journal of Selected Topics in Quantum Electronics 9, 1172.
[2.51] O'Brien S, Welch DF, Parke RA, Mehuys D, Dzurko K, Lang RJ, Waarts R, Scifres D (1993) Operating characteristics of a high-power monolithically integrated flared amplifier master oscillator power amplifier. IEEE Journal of Quantum Electronics 29, 2052.
[2.52] Stohs J, Bossert DJ, Gallant DJ, Brueck SRJ (2001) Gain, refractive index change and linewidth enhancement factor in broad-area GaAs and InGaAs quantum-well lasers. IEEE Journal of Quantum Electronics 37(11), 1449.
[2.53] Mikulla M (2000) Tapered high-power, high-brightness diode lasers Topics of Applied Physics 78, 265.

[2.54] Kelemen MT, Weber J, Rogg J, Rinner F, Mikulla M, Weimann G (2002) Beam quality and linewidth enhancement factor of ridge-waveguide tapered diode lasers. 18th IEEE International Semiconductor Laser Conference, Garmisch, Germany, 81.
[2.55] Dente GC (2001) Low confinement factors for suppressed filaments in semiconductor lasers. IEEE Journal of Quantum Electronics 37(12), 1650.
[2.56] Mikulla M, Chazan P, Schmitt A, Morgott S, Wetzel A, Walther M, Kiefer R, Pletschen W, Braunstein J, Weimann G (1998) High-brightness tapered semiconductor laser-oszillators and amplifiers with low modal gain epilayer-structures. IEEE Photonic Technological Letters 10(5), 654.
[2.57] Lang RJ, Hardy A, Parke R, Mehuys D, O'Brien S, Major J, Welch D (1993) Numerical analysis of flared semiconductor laser amplifiers. IEEE Journal of Quantum Electronics 29, 2044.
[2.58] Al-Muhanna A, Mawst LJ,Botez D, Garbuzov DZ, Martinalli RU, Connolly CJ (1997) 14.3 W quasi-continuous wave front-facet power from broad-waveguide Al-free 970 nm diode lasers. Applied Physics Letters 71, 1142.
[2.59] Kelemen MT, Rinner F, Rogg J, Wiedmann N, Kiefer R, Walther M, Mikulla M, Weimann G (2002) High-power, high-brightness ridge-waveguide tapered diode lasers at 940 nm. SPIE Proceedings 4648, 75.
[2.60] Mikulla M, Kelemen MT, Walther M, Kiefer R, Moritz R, Weimann G (2001) High-power 980 nm laser diodes by MBE. SPIE Proceedings 4580, 11.
[2.61] Kelemen MT, Weber J, Rinner F, Rogg J, Mikulla M, Weimann G (2003) High-brightness 1040 nm tapered diode lasers. SPIE Proceedings 4947, 252.
[2.62] Kelemen MT, Weber J, Kallenbach S, Pfahler C, Mikulla M, Weimann G (2004) Astigmatism and beam quality of high-brightness tapered diode lasers. SPIE Proceedings 5452, 233.